Bulletin of Earthquake Engineering
https://doi.org/10.1007/s10518-026-02565-y

ORIGINAL ARTICLE

Blind-prediction of the dynamic behavior of 3D-printed masonry-like structures under shake-table loading via a high-fidelity numerical modeling approach

Amirhossein Ghezelbash[1] · **Abide Aşıkoğlu**[1] · **Antonio Maria D'Altri**[2] · **Satyadhrik Sharma**[3] · **Francesco Messali**[1]

Received: 5 April 2026 / Accepted: 20 June 2026

Abstract

This paper presents a modeling approach for high-fidelity blind-prediction of dynamic responses of 3D-printed masonry-like structures, as part of a contest organized by Pacific Earthquake Research Center (PEER) for simulating shake table tests on 29 identical ∏-shaped 1:15-scaled sand-based 3D-printed specimens, each subjected to a different earthquake. The contest challenged participants to predict experimental outcomes without access to test results. Leveraging their modeling approach originally developed for regular masonry, the authors proposed an innovative methodology to simulate these structures, implementing extensions to overcome challenges such as representing their continuum nature within a discrete block-and-joint framework and simulating their small-scale response via 1:1-scale counterparts. The numerical model blind-predicted the experimental outcomes with highest accuracy among participants. Parametric studies, before and after access to modal characteristics, showed the importance of such information for simulation accuracy, and the ability of the approach to investigate variability of dynamic responses in complement to physical tests.

Keywords Masonry · Seismic assessment · Numerical modeling · Dynamic analysis · 3D-printing · Blind-prediction

✉ Amirhossein Ghezelbash
a.ghezelbash@tudelft.nl

1 Faculty of Civil Engineering and Geosciences, Delft University of Technology, Delft, The Netherlands

2 Department of Civil, Chemical, Environmental, and Materials Engineering, University of Bologna, Bologna, Italy

3 Reliable Structures Section, Netherlands Organisation for Applied Scientific Research (TNO), Delft, The Netherlands

Published online: 09 July 2026

1 Introduction

Masonry structures are among the most widely used forms of construction, owing to their accessibility, affordability, and ease of implementation (Hendry 2001). Constructed from readily available materials, they are commonly found in both historic and contemporary buildings across diverse regions (Frankie et al. 2013). Despite these advantages, masonry walls possess limited out-of-plane (OOP) strength, rendering them particularly susceptible to dynamic loads such as those generated by earthquakes (Frankie et al. 2013). This intrinsic vulnerability presents significant challenges to ensuring seismic safety (Moon et al. 2014; p. 1991; Penna et al. 2014; Oyarzo-Vera and Griffith 2009; D'Ayala and Paganoni 2011). Consequently, considerable research efforts have been directed towards experimentally investigating their seismic performance, although such studies account for a smaller proportion of the literature than studies on seismic in-plane IP behavior (Chong 1993; Van der Pluijm 1999; Liang 1996; Derakhshan et al. 2018; Bui and Limam 2014; Griffith et al. 2007; Padalu et al. 2020; Damiola et al. 2018; Vaculik and Griffith 2018; Graziotti et al. 2016, 2019; Candeias et al. 2016a; Simsir et al. 2004; Penner and Elwood 2016; Moshfeghi et al. 2024; Sharma et al. 2020).

Record-to-record variability, i.e., the inherent differences in structural behavior arising from variations in ground motion characteristics, poses additional challenges in understanding the seismic response of masonry walls (Caicedo et al. 2024). In one- and two-way OOP bending failure modes, minor differences in intensity and spectral characteristics of the motion can drastically influence response in terms of crack patterns and failure mechanisms as well as the predicted collapse intensities (Ghezelbash et al. 2025; Kadysiewski and Mosalam 2009; Penner and Elwood 2016; Cima et al. 2024; Giordano et al. 2021, 2021; Nale et al. 2023; Kaya et al. 2023). Without a robust quantification of this variability, seismic risk estimates based on a limited number of ground motions may either overestimate safety or underestimate the likelihood of failure (Gesualdi et al. 2020; Dauda et al. 2024; Sumerente et al. 2020). While existing studies largely focus on developing fragility curves or generalized vulnerability assessments, few studies investigate the effects of varying seismic records while keeping other structural properties constant (Cima et al. 2023, 2024). Laboratory experiments on dynamic OOP wall behavior typically employ a limited set of earthquake records, restricting the ability to reliably assess record-to-record variability (Graziotti et al. 2016; Moshfeghi et al. 2024; Sharma et al. 2020; Losanno et al. 2023; Vemuri et al. 2022; Anić et al. 2020; Mucedero et al. 2022; Simsir et al. 2004; Griffith et al. 2004; Giaretton et al. 2016; Vaculik 2012; Candeias et al. 2016b). Similarly, numerical studies on masonry OOP dynamics rarely conduct systematic sensitivity analyses on the effects of loading signals (Ghezelbash et al. 2025; Malomo et al. 2020; Tondelli et al. 2016). Only analytical models, primarily simplified representations such as rigid-block mechanisms, once experimentally and numerically validated, are used to capture aspects of record-to-record variability (Baek et al. 2024; Kallioras et al. 2022; Sivori et al. 2022; Losanno et al. 2023; De Felice and Giannini 2001). Consequently, comprehensive experimental campaigns and robust numerical modeling approaches that adopt many different earthquake records for the loading of their specimens are essential to fill this gap and enhance the seismic assessment of masonry structures.

To deepen the understanding of record-to-record variability in masonry dynamics, an experimental campaign has been conducted by the Pacific Earthquake Engineering Research

Center (PEER, USA), the National Technical University of Athens (NTU Athens, Greece), and the Eidgenössische Technische Hochschule (ETH Zürich, Switzerland) (Pacific Earthquake Engineering Research Center PEER 2025). In this campaign, 29 identical 1:15-scale physical models of 3D-printed masonry-like specimens were fabricated, and each was subjected to a unique dynamic ground motion from past earthquake events via shake table testing at the Geotechnical Centrifuge Center of ETH Zürich (Elmorsy et al. 2026). The specimens are masonry-like because they are not constructed from masonry units and mortar; instead, they replicate masonry typology through the inclusion of dry cuts in their volume. The 29 loading signals used in the tests differ in terms of both intensity and spectral content, leading to the investigation of record-to-record variability under the influence of both parameters. A blind-prediction contest was organized within this campaign to evaluate the current capabilities of numerical models in predicting the behavior of these specimens across all 29 tests, to assess their effectiveness in capturing record-to-record variability. Participants were only provided with the mechanical behavior of the sand-based material used to construct the specimens (Phase 1 of the blind prediction contest, as described in Sect. 2.5) and, at a later stage (Phase 2), the modal characteristics of the specimens. They were tasked with predicting the collapse probability and OOP deformation demands observed during the experiments. This initiative directly supports the need for reliable numerical modeling strategies (e.g., (Malomo et al. 2020; Vanin et al. 2020; Kesavan and Menon 2022, 2023; Malomo and DeJong 2022; Lourenço 2000; Noor-E-Khuda 2021; Noor-E-Khuda et al. 2016; Selby and Vecchio 1993; Rots et al. 2016; Sharma et al. 2021; Mohyeddin et al. 2013; D'Altri et al. 2018; Xie et al. 2021; Oktiovan et al. 2024; Macorini and Izzuddin 2011; Nie et al. 2023)) capable of simulating masonry dynamics while accounting for its chaotic nature and dependency on different variables. The blind prediction contest enabled participants to assess the accuracy of their numerical models against the dynamic behavior of this large set of physical specimens subjected to real seismic ground motions. Additionally, it enabled the calibration of numerical models developed through this process, which could offer reliable alternatives to physical testing, extending existing knowledge on dynamic masonry behaviors by exploring structural and loading scenarios beyond those previously tested in laboratory settings (Lourenço 2004; Girardi et al. 2021).

To contribute to these objectives, the numerical modeling approach previously developed by the authors (Ghezelbash et al. 2025b) for high-fidelity simulation of dynamic one- and two-way OOP bending behavior in unreinforced masonry walls is used to participate in the blind-prediction contest. The modeling approach is extended on several fronts compared to its original form to allow applicability to the specimens tested in the PEER campaign. First, the modeling approach, used until now to simulate the dynamic response of single walls or return walls with small flanges, is extended to the sub-structure dynamics, where several walls with openings and specific wall-wall connection details are modeled. Second, since the original approach has been developed within a "discrete" block-and-joint framework, additional modeling steps are formulated to allow it to represent the "continuum-like" typology of the 3D-printed specimens. Third, since the approach has been used to simulate 1:1-scale specimens until now, a conversion procedure is devised to allow simulation of the 1:15-scale tested specimens. In fact, this study marks the first instance in the literature where a block-based modeling approach is employed to simulate 3D-printed structures, and where the dynamic response of scaled specimens is simulated within a full-scale setting. Fourth, a multi-variational approach is adopted in the study by which the simulations are conducted with different variations of loading assumptions, mechanical properties (both elastic and nonlinear), and damping characteristics from those considered in the experimental specimens, offering complementary insights into the influence of different parameters on the record-to-record variability of masonry OOP dynamic response. This paper reports on these numerical modeling efforts and blind prediction results, and is organized as follows. After the introductory background, Sect. 2 introduces the PEER experimental campaign, detailing the testing conditions and outlining the structure of the blind prediction contest. Section 3 presents the modeling strategy used in this study, emphasizing the approach adopted to extend it to the 3D-printed typology and 1:15 similitude scale of the PEER specimens. In Sect. 4, a parametric analysis is formulated to account for the uncertainties influencing the experimental outcomes by introducing different model variations. Section 5 presents and discusses the simulation results. Section 6 presents a comparison between the response of this study to the blind-prediction contest and the real experimental outcomes published after the contest (Elmorsy et al. 2025). Finally, Sect. 7 summarizes the key findings and offers concluding remarks, highlighting directions for future research.

2 Experimental benchmark campaign

This section introduces the experimental campaign (Elmorsy et al. 2026) used as the benchmark for the PEER blind prediction contest (Pacific Earthquake Engineering Research Center PEER 2015). The objective of the campaign has been to investigate the record-to-record variability in the dynamic behavior of masonry-like structures through unidirectional shake table testing. A total of 29 identical 3D-printed masonry-like specimens are tested, each subjected to a different ground motion applied at their base. Detailed descriptions of the specimens, test set-up and instrumentation, and the loading protocol used in the experimental campaign as well as the procedure of the blind-prediction contest are provided in the following sub-sections. The information provided here is collected only from the data made available to participants of the blind prediction contest.

2.1 Geometry of specimens

The overview of the geometry of the experimental specimens is provided in Fig. 1. Each specimen represents a 1:15-scaled model (scale factor $\lambda_L = 1/15$) of a $\sqcap$-shaped masonry-like sub-structure, manufactured via sand-based 3D printing utilizing binder-jet technology (Del Giudice et al. 2024). The model sub-structures each consist of three walls: one wall oriented perpendicular to the loading direction (referred to as the “main wall” or “OOP wall”) and two walls parallel to the loading direction (referred to as the “return walls” or “flanges”). The main wall has a total (exterior edge-to-edge) length of 242.60 mm, while each of the return walls extends 161.40 mm from their back edge to the face of the main wall. The return walls are rectangular with a constant height of 150.40 mm, whereas the main wall includes an isosceles triangular gable at its top. The gable starts at an elevation of 150.40 mm at both ends of the wall and reaches a total height of 191.80 mm from the base at its mid-span, corresponding to a net gable height of 41.40 mm. The thickness of all three walls is 15.00 mm.

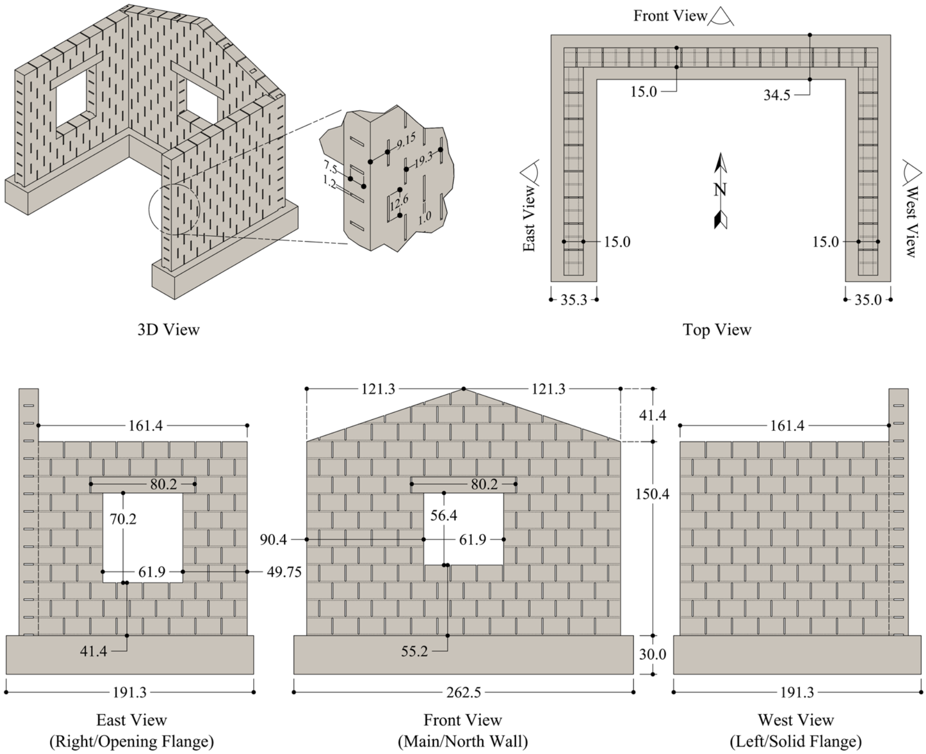

Fig. 1 Geometrical dimensions of sub-structures tested in PEER experimental campaign. Dimensions in mm. The figure is adapted based on information provided during the blind-prediction contest (Pacific Earthquake Engineering Research Center PEER 2015)

Although each specimen is constructed as a continuous body, vertical and horizontal dry cuts are introduced to replicate the unit-by-unit typology of masonry. Specifically, vertical cuts with a thickness of 1.00 mm are made through the entire thickness of the walls to represent vertical joints (head joints) of non-contacting masonry units, simulating a 19.30 mm length for the full units and 9.15 mm for half-units. Additionally, horizontal cuts with a height of 1.20 mm are made across half the thickness of the walls (7.50 mm) to represent horizontal mortar joints (bed joints), replicating units with a height of 12.60 mm. Consequently, the bed joints only connect the side edges of the units with a thickness of 3.75 mm per side, replicating how masonry units with vertical holes are connected in practice. A full connection across the entire wall thickness is considered between the main wall and the flanges (i.e., no cuts are applied at these connections).

Each specimen includes two window openings: one for the main wall and one for the left return wall. The main wall window has a length of 61.90 mm and a height of 56.40 mm and is positioned symmetrically at the mid-length of the wall, starting at four-unit-rows (55.20 mm) above the base. The window of the left return wall shares the same length as the main wall window but has a height of 70.20 mm. It starts at 49.75 mm from the free edge of the flange (measured exterior edge-to-edge) and at three-unit-rows (41.40 mm) above the base. A lintel, made of the same sand-based 3D-printing material as the rest of the specimen, is placed above each window, with dimensions matching the units in height and thickness. Lintels are 80.20 mm long and extend 9.15 mm beyond each end of the windows, corresponding to the length of a half-unit at each side.

2.2 Experimental set-up

The test set-up used for the dynamic loading of the specimens is shown in Fig. 2. Each specimen is printed together with a base which follows the same ∏-shaped planar layout as the sub-structure and has a 30 mm height. The base extends 262.6 mm in length parallel to the main wall and 191.4 mm in length along the direction of the flanges. For the tests, each specimen is secured to the shake table using steel plates that enclose approximately one-third of the height of the base, preventing relative displacement between the base and the shake table, including uplift, during tests. The main wall of each specimen is assumed to face North, and the flanges extend towards South.

2.3 Loading protocol

A total of 29 unidirectional shake table tests have been conducted to comprehensively investigate the sensitivity of the dynamic response of masonry models to the characteristics of the loading signals. Each test is performed on one separate specimen, in pristine (as-built) condition, by applying one of the input signals listed in Table 1. The signals are selected from the PEER NGA-West2 ground motion database (Ancheta et al. 2014) and demonstrate a wide range of intensity levels and spectral characteristics.

To maintain a 1:1 similitude between the stresses and strains ($\lambda_\sigma = \lambda_\varepsilon = 1$) of the scaled specimens (referred to as "models" in this paragraph) and those of their theoretical full-scale counterparts (referred to as "prototypes" in this paragraph), the raw loading signals are modified for the tests following the Cauchy similitude law (Harris and Sabnis 1999). The Cauchy similitude law (Harris and Sabnis 1999) prescribes adjustments to the loading intensity and spectral content of dynamic loads while preserving the same material properties as the prototype. Firstly, since the density of the material used in the models remains identical to that of the prototypes, the mass of the models decreases proportionally to the reduction in their volume ($\lambda_m = \lambda_V = \lambda_L^3 = 1/15^3$). However, the decrease in the surface area of the models

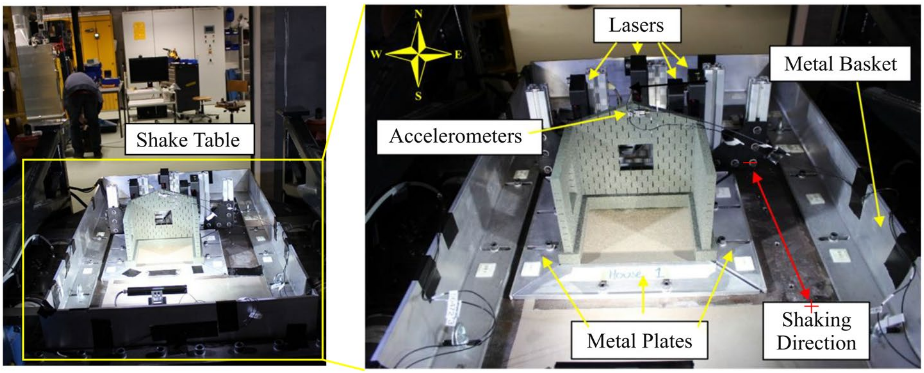

Fig. 2 Experimental set-up used for the testing of PEER sub-structures (Pacific Earthquake Engineering Research Center PEER 2015; Elmorsy et al. 2026)

Table 1 Ground motion signals used for the shake table testing of each specimen

Test #	Specimen Name	Signal Source		Recorded Motion Properties[ii]	
		Earthquake Event	PEER Database[i] File	PTA[iii] [g]	Duration [s]
1	House_1	Northridge-01 (USA, 1994)	RSN1004_NORTHR_SPV360	18.24	10.0
2	House_2	Northridge-01 (USA, 1994)	RSN1048_NORTHR_STC090	13.24	31.0
3	House_3	Northridge-01 (USA, 1994)	RSN1048_NORTHR_STC180	17.06	15.0
4	House_4	Northridge-01 (USA, 1994)	RSN1063_NORTHR_RRS318	8.24	20.0
5	House_5	Northridge-01 (USA, 1994)	RSN1086_NORTHR_SYL360	23.57	10.0
6	House_6	Kobe (Japan, 1995)	RSN1111_KOBE_NIS000	14.35	13.0
7	House_7	Kobe (Japan, 1995)	RSN1111_KOBE_NIS090	15.66	18.0
8	House_8	Chi-Chi (Taiwan, 1999)	RSN1244_CHICHI_CHY101-E	15.94	19.0
9	House_9	Friuli-01 (Italy, 1976)	RSN125_FRIULI.A_A-TMZ000	13.34	15.0
10	House_10	Duzce (Turkey, 1999)	RSN1602_DUZCE_BOL000	17.00	16.0
11	House_11	Manjil (Iran, 1990)	RSN1633_MANJIL_ABBAR–L	19.81	18.0
12	House_12	Imperial Valley-06 (USA, 1979)	RSN169_IMPVALL.H_H-DLT262	23.27	16.0
13	House_13	Hector Mine (USA, 1999)	RSN1787_HECTOR_HEC000	19.71	15.0
14	House_14	Nahanni (Canada, 1985)	RSN495_NAHANNI_S1010	21.79	15.0
15	House_15	Nahanni (Canada, 1985)	RSN495_NAHANNI_S1280	23.29	15.0
16	House_17	Darfield (New Zealand, 2010)	RSN6888_DARFIELD_CCCCN26W	11.32	10.5
17	House_18	Darfield (New Zealand, 2010)	RSN6888_DARFIELD_CCCCN64E	12.07	10.5
18	House_19	Superstition Hills-02 (USA, 1987)	RSN721_SUPER.B_B-ICC000	15.44	10.0
19	House_20	Superstition Hills-02 (USA, 1987)	RSN723_SUPER.B_B-PTS315	16.88	18.0
20	House_21	Superstition Hills-02 (USA, 1987)	RSN725_SUPER.B_B-POE270	13.79	10.0
21	House_22	Superstition Hills-02 (USA, 1987)	RSN725_SUPER.B_B-POE360	12.27	15.0
22	House_23	Loma Prieta (USA, 1989)	RSN752_LOMAP_CAP000	11.19	15.0
23	House_24	Loma Prieta (USA, 1989)	RSN767_LOMAP_G03000	13.12	5.0
24	House_27	Cape Mendocino (USA, 1992)	RSN825_CAPEMEND_CPM000	19.51	35.0
25	House_28	Landers (USA, 1992)	RSN848_LANDERS_CLW-LN	19.28	8.0
26	House_29	Northridge-01 (USA, 1994)	RSN953_NORTHR_MUL009	22.31	9.0
27	House_30	Northridge-01 (USA, 1994)	RSN953_NORTHR_MUL279	25.04	8.0
28	House_31	Northridge-01 (USA, 1994)	RSN960_NORTHR_LOS000	25.92	10.0
29	House_32	Northridge-01 (USA, 1994)	RSN960_NORTHR_LOS270	26.98	10.0

[i] The NGA-West2 database available at (Ancheta et al. 2014)

[ii] Extracted from the recordings of the accelerometer connected to the shake table during dynamic tests

[iii] Peak Table Acceleration

relative to the prototypes is only two orders of magnitude ($\lambda_A = \lambda_L^2 = 1/15^2$), which disrupts the proportionality of stresses ($\lambda_\sigma = \lambda_a \lambda_m / \lambda_A$). The Cauchy similitude law tackles this by upscaling the intensity of the applied loading, controlled by the acceleration data in the case of dynamic signals, in accordance with the inverse of the scale factor used for the geometry

(λ_A=λ_L^{-1} = 15). Secondly, maintaining a 1:1 similitude for the Elasticity modulus between the model and prototype (λ_E = 1), given that the same material is used in both, results in a lower elastic stiffness for the model compared to the prototype (λ_k=$\lambda_E\lambda_L$ = 1/15). Thus, the natural frequencies of the model become significantly higher than those of the prototype (λ_f = $\sqrt{\lambda_k/\lambda_m}$ = 15) as stiffness reduction is not proportional to the mass reduction. To account for this, Cauchy law downscales the spectral content of the dynamic loads, controlled by the time intervals between each two points in the loading signals, by a factor equal to that applied to the geometry (λ_T=λ_L = 1/15).

The scaled loading signals, modified in intensity and time content according to the λ_a = 15 and λ_T = 1/15 scaling factors, respectively, are applied to the tested specimens in a direction perpendicular to the main walls (North-South direction in Fig. 2). The positive direction of loading aligns towards the free ends of the flanges and away from the main wall (South). The Peak Table Acceleration and loading duration of each test is listed in Table 1. Moreover, the one-by-one illustration of the motions recorded at the shake table in the direction of loading during each of the 29 tests is presented in the Appendix to facilitate comparison with their counterparts processed in this study. It should be noted that no additional vertical loads, beyond the self-weight of the specimens, have been applied prior to dynamic loadings.

2.4 Instrumentation

The response of the specimens during the shake table tests is recorded using the sensor layouts shown in Fig. 3. In all tests, one pair of accelerometers is mounted at the top of the gable (typical configuration): one to record IP motions (referred to as the "IP" accelerometer) and the other for OOP motions (called the "OOP" accelerometer). Additionally, the movement of the top and sides of the gable is monitored via lasers. For tests 16, 17, 18, 19, and 23, a refined instrumentation is adopted, where two additional pairs of accelerometers are installed at the top corners of the free edges of each flange, and one extra OOP accelerometer is positioned at the bottom right corner of the window in the main wall. The mass

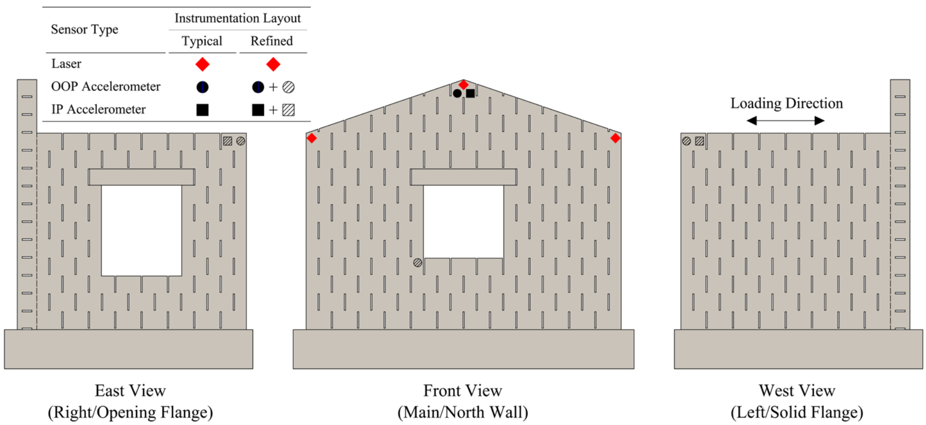

Fig. 3 Layout of the instrumentations used to record the dynamic response of the sub-structures in the tests. Refined instrumentation layout is used in tests 16, 17, 18, 19, and 23. The figure is drawn based on information provided during the blind-prediction contest (Pacific Earthquake Engineering Research Center PEER 2025; Elmorsy et al. 2026)

of each IP accelerometer (m_{IP}) is 1.77 grams, while the mass of each OOP accelerometer (m_{OOP}) is 2.59 grams, both values being comparable to the mass of a masonry unit.

2.5 Blind-prediction contest

The blind-prediction contest was organized in two phases. In the first phase (hereafter referred to as "Phase 1"), the geometrical configuration and loading specifications of the specimens, along with characterization test results (Del Giudice et al. 2024) for the sand-based material used in constructing the sub-structures were made available. The primary objective of Phase 1 was to assess the capability of existing numerical modeling approaches in predicting the dynamic behavior of masonry structures when only material properties and component-level behaviors were known. It should be noted that a video which showed a proof-of-concept shake table experiment conducted on a sample sub-structure, prior to the 29 experiments designed for the blind-prediction contest, was also published by the organizers along with the Phase 1 data. This video was intended to help participants better understand the expected structural response. In the second phase (referred to as "Phase 2"), additional data obtained from ambient vibration testing of the sub-structures were provided to the participants, allowing for further calibration of the numerical models to reflect the modal characteristics of the tested specimens. The goal of Phase 2 was to investigate the effectiveness of using ambient vibration measurements as a basis for refining numerical models. As shown in Fig. 4a, the vibration test was performed on one of the 29 specimens by applying 11 hammer impacts to the loading system in the direction parallel to the dynamic loading applied during the shake-table tests (North-South). The resulting accelerations at various locations on the specimen were recorded using the IP and OOP accelerometers illustrated in Fig. 4b. While the complete time-histories of the recorded accelerations were made available to the participants during Phase 2, they are here omitted for brevity. In both phases, the contestants were asked to provide their prediction for the status of the specimen (collapsed or not collapsed) together with the maximum OOP displacement recorded at the top of the gable during each of the 29 shake table tests. Submissions were evaluated independently by comparing the predicted and experimentally observed probability of collapse, computed as the number of collapsed specimens normalized by the total (29) number of tests, as well as by comparing the cumulative distribution functions (CDFs) of the predicted OOP deformation demands with those derived from experimental observations. Submissions for each phase were evaluated independently, with a winning entry announced for each respective phase.

3 Numerical modeling strategy

The high-fidelity block-based numerical modeling approach originally developed by the authors in (Ghezelbash et al. 2025b) and implemented into the Abaqus software (Hibbitt et al. 2011) is herein adopted to simulate the PEER experiments described in Sect. 2. Given that the approach has been comprehensively described in several previous publications (Ghezelbash et al. 2025a, b), its full reiteration is intentionally omitted here for the sake of readability. Accordingly, this section focuses on the specific considerations and modifications implemented to adapt the modeling approach to the PEER sub-structures, with particular

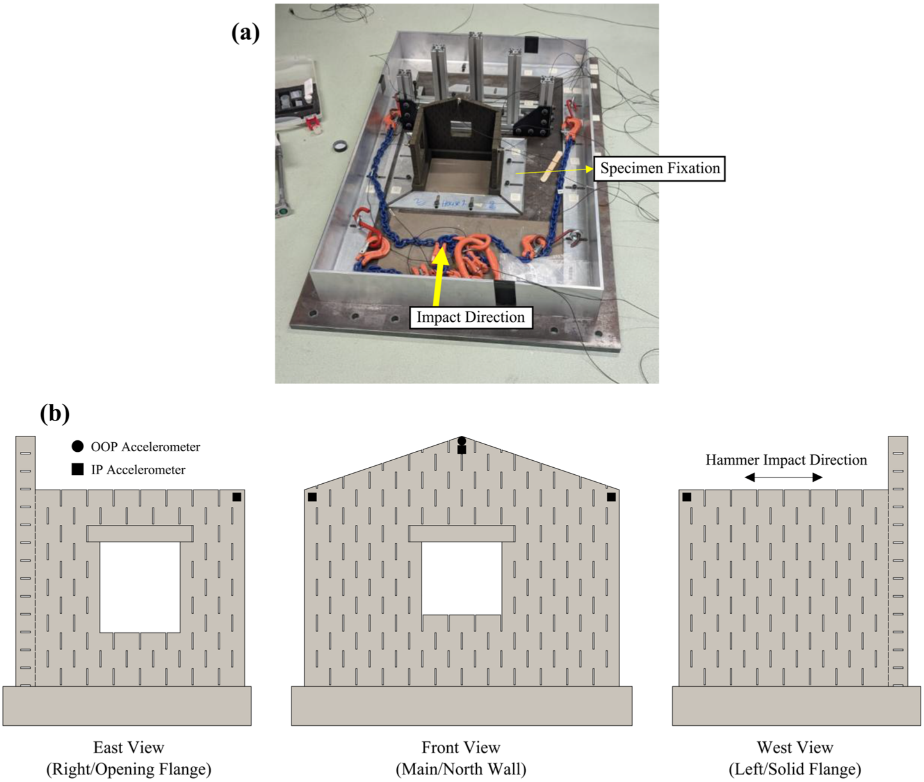

Fig. 4 Overview of the modal identification test: set-up (**a**) and instrumentation (**b**). The figure is drawn based on information provided during the blind-prediction contest (Pacific Earthquake Engineering Research Center PEER 2025; Elmorsy et al. 2026)

attention to capturing their small-scale geometries and continuum 3D-printed nature. The methodology adopted for geometrical representation, material calibration, dynamic loading application, and analysis set-up are detailed in the following sub-sections. It is important to note that the information provided herein pertains to the numerical modeling activities conducted during Phase 1 of the contest. The updates applied to the numerical models for Phase 2 are presented separately in Sect. 4.

3.1 Geometry and finite element discretization

The geometry of the specimens is recreated in 3D and includes both the sub-structures and their base as depicted in Fig. 5a. For simplicity, the shake table and the components connecting it to the specimens, as well as the accelerometers are not modeled. Nevertheless, the latter is implicitly included in the model as explained in Sect. 3.2. To keep the finite element discretization simple, the triangular units of the gable are replaced with simplified rectangular blocks, labeled "G_i" in the figure with "i" indicating the block number within the gable.

In addition to the simplifications mentioned above, an essential step was taken to address the limitations associated with numerically modeling specimens scaled according to the

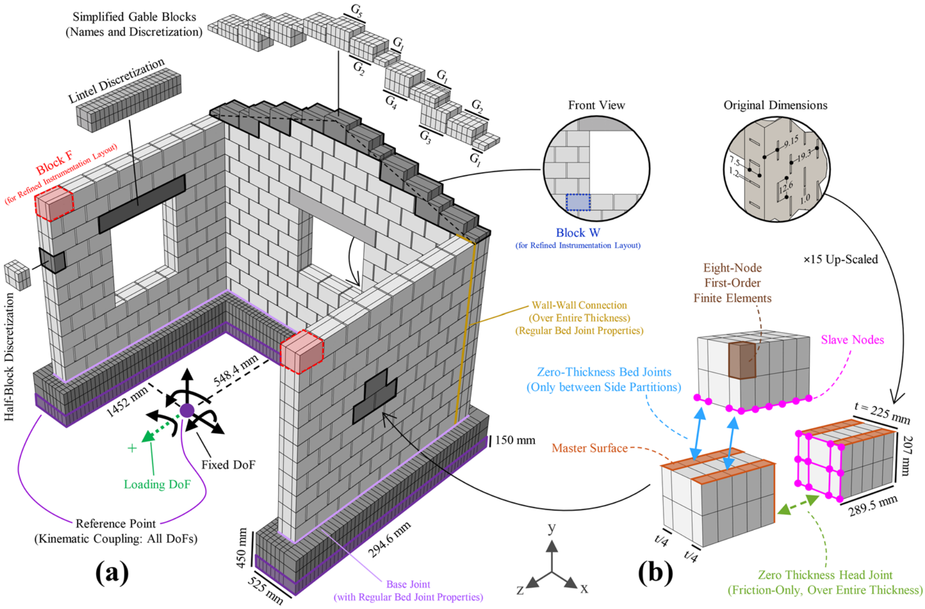

Fig. 5 Overview of the numerical models: assembly (**a**) and typology (**b**). The full-scale counterparts of the sub-structures are simulated, i.e., all geometrical dimensions are upscaled by 15. The abbreviation "DoF" refers to degrees of freedom

Cauchy similitude law (Harris and Sabnis 1999). Specifically, the tested specimens exhibit natural frequencies 15 times higher than those of their theoretical full-scale counterparts across all vibration modes. Consequently, extremely small time-steps would be required in the dynamic solver used in this study (Hibbitt et al. 2011) to perform the analyses, resulting in prohibitively slow simulations that could not be completed within the timeframe of the contest. To overcome this, the decision was made to simulate a 1:1 full-scale representation of the specimens instead of their as-built scaled geometries. Accordingly, all geometrical dimensions of the specimens are up-scaled by a factor of $\lambda_L^{-1} = 15$ in the numerical models.

Another important step was to find a correct representation of the typology of the specimens. Specifically, while the tested sub-structures are constructed as homogeneous continua with no full discontinuities between the units, the modeling approach adopted in this study (Ghezelbash et al. 2025b) has been developed for traditional brick masonry and represents it in a discrete meso-scale (or simplified micro-scale) manner using expanded blocks and zero-thickness joints. Consequently, the geometry of the specimens is adjusted in the numerical models to convert them into discretized unit-by-unit assemblies, as depicted in Fig. 5b. The blocks, half-blocks, and lintels are extended in height by the thickness of the dry cuts (15 mm) in the numerical models, and the explicit simulation of horizontal cuts is omitted to avoid unnecessarily refined mesh discretization. To reproduce the bed joint connections, the thickness dimension ($t = 225$ mm) of the expanded blocks and half-blocks is partitioned into three sections with a t/4–t/2–t/4 division, and zero-thickness connections simulating bed joints are only implemented along the two exterior t/4-thick partitions. The conversion of the continuum-like 3D-printed typology to a discrete block-and-joint assembly is allowed by the type of failure mechanism expected from the tested specimens. In particular, the proof-of-concept video published in the Phase 1 data shows that the majority of damage occurs in the form of horizontal and vertical cracks passing through bed and head joints, rather than diagonal cracks involving the units. Moreover, no crushing is observed in the video, and crushing is also not expected to have occurred in the main tests, as the specimens were not subjected to additional vertical loading.

Concerning discretization, the expanded blocks, half-blocks, lintels, simplified gable blocks, and the base are idealized as continuum bodies and discretized using eight-node hexahedral finite elements. A discretization scheme of 5 elements in length, 2 in height, and 3 in thickness (one per thickness partition) is employed for the expanded blocks. Comparable element sizes are used for other components, with half-blocks containing 3 elements in length and lintels containing 21. The G_1 blocks in the gables, due to their small size, are assigned 2 elements in length and 1 element in height, which still allows for proper simulation of their deformations. The base of the specimens is partitioned into smaller segments along its thickness and length to ensure consistency of its discretization with that of the expanded blocks and half-blocks. Additionally, the base is divided into two partitions over its height: the bottom part, representing one-third of the total height, is used for the prescription of boundary conditions, and the top part is left to deform freely, following the connection scheme used in the tests (see Sect. 2.2). The bottom part is discretized into 1 element in height and the top part into 2 elements to accurately capture its deformation.

The block-to-block, wall-to-wall, and wall-base connections at the zero-thickness joints are modeled using a contact algorithm based on the penalty method and master-slave formulation (Hibbitt et al. 2011; Weyler et al. 2012), where each discrete point of the slave surface is connected to several points on the master surface. The contact points coincide with the vertices of the hexahedral elements. The longitudinal and thickness discretization scheme adopted for the different components has been shown in previous studies by the authors (Ghezelbash et al. 2023, 2025a, b) to provide sufficient contact points to reliably capture both IP and OOP responses at the joints.

3.2 Constitutive mechanical assumptions

The constitutive behavior depicted in Fig. 6 is adopted for the zero-thickness joints, as detailed in (Ghezelbash et al. 2025a, b) consisting of a cohesive response in tension and a non-dilatant cohesive-frictional response in shear. In the general form of the numerical modeling approach adopted (Ghezelbash et al. 2025b), the expanded blocks exhibit nonlinear behavior in both tension and compression, simulating the tensile response of masonry

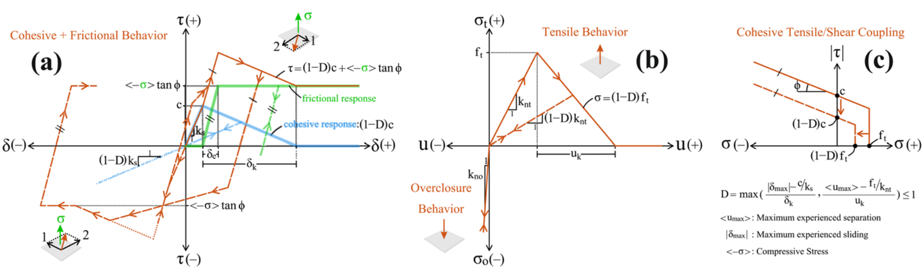

Fig. 6 Constitutive behavior of the zero-thickness joints: response parallel (**a**) and normal (**b**) To the joint plane, along with coupling of cohesive tensile and shear responses (**c**)

units and the compressive response of masonry-like assemblies, respectively. The zero-thickness joints exhibit nonlinear tensile and shear behaviors based on the relative displacement of the master surfaces with respect to slave nodes, capturing the tensile and shear response of the mortar and unit-mortar interfaces, respectively. However, given that the collapse mechanism of the PEER sub-structures is expected to exclusively involve the joints due to low vertical stresses, a linear elastic response is assumed for blocks, half-blocks, base, and lintels in the numerical models. Although the proof-of-concept video published in the Phase 1 data shows minor tensile cracking at the corners of the units, such damage occurs because of the propagation of cracks from head to bed joints, and vice versa, rather than the failure of the blocks themselves. Therefore, the use of elastic blocks is expected to only minorly affect crack propagation. For the joints, the nonlinear constitutive behaviors detailed in (Ghezelbash et al. 2025a, b), consisting of a cohesive response in tension and a non-dilatant cohesive-frictional response in shear, are implemented. The monotonic tensile behavior of the joints is characterized by an elastic regime followed by a post-peak regime with linear softening until complete loss of strength. Their cohesive shear response follows a similar constitutive behavior, while their frictional shear response is modeled via a constant friction developed after an initial elastic slip phase. The cyclic response of the joints includes secant unloading-reloading with stiffness degradation proportional to strength loss, as well as elastic unloading-reloading in shear. The tensile and cohesive shear responses are coupled, such that softening in one results in a proportional loss of strength in the other. In overclosure, the joints have a linear elastic behavior.

Following the calibration procedure outlined in (D'Altri et al. 2019), the input parameters governing the constitutive behavior of the blocks and joints are derived from simulations of the PEER material characterization tests provided in the Phase 1 data of the PEER contest (Del Giudice et al. 2024). Specifically, the Elasticity modulus ($\mathrm{E_m}$) of the blocks is calibrated using uniaxial compression tests on wallet specimens, while a large value is assigned to the normal stiffness of the joints in overclosure ($\mathrm{k_{no}}$) to avoid significant block interpenetration. The density (ρ_m) and Poisson's ratio (ν_m) of the blocks is adopted directly from the contest data as the properties of masonry assemblies. The base and lintels are assigned with the same material properties of the blocks. The tensile stiffness of the joints ($\mathrm{k_{nt}}$) is assumed equal to $\mathrm{k_{no}}$, while their cohesive tensile strength ($\mathrm{f_t}$) is calibrated via the simulations of four-point bending tests on the reference material. Shear properties, including cohesive elastic stiffness ($\mathrm{k_s}$), frictional elastic slip threshold (δ_e), shear cohesive strength (c), friction coefficient ($\tan\phi$), and the length of the shear softening regime (δ_k), are characterized by simulating IP experimental tests performed on single walls under cantilever boundary conditions and two levels of vertical load. The length of the tensile softening regime ($\mathrm{u_k}$) is assumed equal to δ_k. Identical properties are assumed for bed joints, base joints, and wall-wall connection joints, as these represent a discretized idealization of the same material nonlinear tensile and shear response. In the head joints, dry contact with a no-overclosure friction-only response is assumed between the vertical faces of adjacent blocks, half-blocks, or lintels across the entire wall thickness. This prevents interpenetration in the event of contact, although such contact is unlikely due to the large separation between the blocks. The frictional and overclosure behavior of the head joints is characterized by the same mechanical properties as those assigned to the regular bed joints.

The results of material-level numerical simulations, preformed in a displacement-controlled nonlinear static analysis framework, are presented in Figure 7 and compared with the corresponding experimental data. The numerical load-deformation responses include both reference simulations, performed using the calibrated material properties collected in Table 2, and additional simulations incorporating variations in model settings. The reference simulations are depicted with blue dashed lines, while the variations are shown using different colors and line styles. The experimental responses are illustrated with solid gray lines. The numerical deformed shapes correspond to the reference set-up. Anyhow, simulations with varied parameters exhibit similar deformation patterns, with no significant differences. The

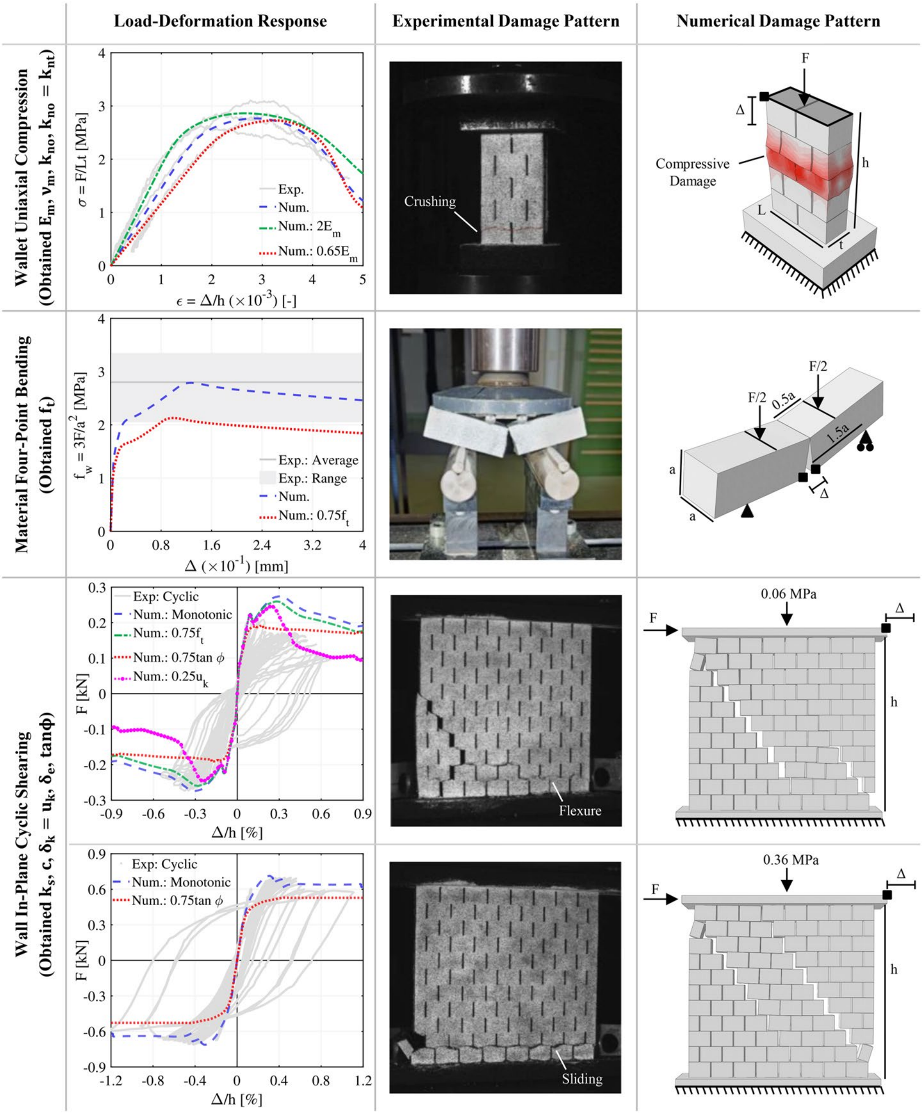

Fig. 7 Results of material characterization simulations performed for calibrating the constitutive mechanical behavior of the numerical sub-structures. The load-deformation curves of reference numerical models with calibrated parameters are shown with dashed blue lines, and the curves of additional models with different variations of the parameters are shown with other styles and colors

Table 2 Input parameters for mechanical behavior of the numerical models of the sub-structures

Expanded Blocks, Lintels, and Base							
Elastic Behavior		**Density of Gable Blocks**				**Density of Blocks with Sensors**	
$\mathrm{E_m}$ [MPa]	7000.0	$\rho_{\mathrm{m_{G_1}}}\ [\mathrm{kg/m^3}]$		667.5		$\rho_{\mathrm{m_F}}\ [\mathrm{kg/m^3}]$	2425.0
ν_{m} [−]	0.15	$\rho_{\mathrm{m_{G_2}}}\ [\mathrm{kg/m^3}]$		905.1		$\rho_{\mathrm{m_W}}\ [\mathrm{kg/m^3}]$	1982.5
$\rho_{\mathrm{m}}\ [\mathrm{kg/m^3}]$	1335.0	$\rho_{\mathrm{m_{G_3}}}\ [\mathrm{kg/m^3}]$		1254.9		(only in tests 16, 17, 18, 19, and 23)	
		$\rho_{\mathrm{m_{G_4}}}\ [\mathrm{kg/m^3}]$		1013.9			
		$\rho_{\mathrm{m_{G_5}}}\ [\mathrm{kg/m^3}]$		2264.8			
Zero-Thickness joints							
Overclosure Behavior[i]		**Tensile Cohesive Behavior**[ii]		**Shear Cohesive Behavior**[ii]		**Shear Frictional Behavior**[i]	
$\mathrm{k_{no}}\ [\mathrm{N/mm^3}]$	16.1 (241.4^3)	$\mathrm{k_{nt}}\ [\mathrm{N/mm^3}]$	16.1 (241.4[iii])	$\mathrm{k_s}\ [\mathrm{N/mm^3}]$	6.9 (103.2[iii])	$\tan\phi$ [−]	0.85
		$\mathrm{f_t}$ [MPa]	0.97	c [MPa]	0.08	δ_{e} [mm]	0.06 (0.004)
		$\mathrm{u_k}$ [mm]	36 (2.4[iii])	δ_{k} [mm]	36 (2.4[iii])		

[i] Assigned to bed and head joints

[ii] Assigned only to bed joints

[iii] Original values in 1:15-scale simulations of the material tests

block discretization scheme used in these material-level simulations is consistent with that employed in the sub-structure simulations. It is important to note that the uniaxial compression simulations are conducted using nonlinear blocks to capture the crushing behavior of the material, whereas all other simulations are performed with linear elastic blocks, consistent with the sub-structure modelling approach. Information regarding the typical nonlinear behaviors of the blocks used for the compression simulations can be found in (Ghezelbash et al. 2025b). Moreover, although the PEER wall IP experiments are conducted under quasi-static cyclic loading, the numerical simulations adopt a static monotonic pushover protocol due to time constraints. This simplification is deemed acceptable, as monotonic analyses allow correct calibration of the majority of the input parameters governing the shear response of the joints ($\mathrm{k_s}$, δ_e, c, and $\tan\phi$). Moreover, although the calibration of δ_k (here equal to $\mathrm{u_k}$) can be sensitive to the loading protocol, since different variations of this parameter are considered during the calibration simulations and dynamic analyses of the sub-structures (see Sect. 4), this sensitivity is deemed to have been sufficiently addressed in this study.

The reference numerical simulations show an overall good agreement with the experimental outputs in terms of load-deformation (or -displacement) responses (dashed blue lines) and failure patterns. Nevertheless, three main criticalities are observed in Fig. 7. First, substantial variability is found in the experimentally derived values of $\mathrm{E_m}$ and $\mathrm{f_t}$, highlighting the need for a comprehensive treatment of uncertainty in these parameters when modeling the sub-structures. Second, a distinct difference is observed in the behavior of the IP low-pre-compressed wall when loaded in different directions, particularly in the positive direction where a 25% lower strength and more rapid softening compared to the negative regime are observed. This, partially caused by the uncertainties governing experimental setups may also suggest the non-uniform distribution of material properties across the specimen, which may have affected its directional behavior. Hence, it denotes that the uncertainties regarding the nonlinear joint properties, especially $\tan\phi$ and $\mathrm{u_k}$ which govern the response of the low-compressed IP wall, should be considered in the sub-structure simulations. Third, although the failure mechanisms observed in the numerical simulations of the wall IP tests are consistent with those from the reference experiments, differences in the crack pattern are noticeable. This discrepancy may be attributed to the difference in loading protocols, with the numerical simulations employing monotonic loading as opposed to the cyclic loading used in the experiments. Moreover, the potential role of minor spatial variations of material properties not included in the numerical models but potentially present in the experiments, despite the use of a 3D-printing construction technology (Bayrak et al. 2024), is acknowledged. In addition, the simplifications introduced to model the experimental material (which diverts from traditional masonry, as discussed above) may have also led to different outcomes in the experiment than that predicted in the simulation. Overall, the outcomes of the simulations are considered sufficiently accurate, especially for the calibration purpose of this section.

After performing the material-level simulations, three key modifications are implemented in the calibrated input parameters to ensure that the dynamic response of the numerical models aligns with the expected behavior of the experimental specimens. First, the simplified rectangular blocks at the top of the gables in the numerical models are assigned updated densities so their mass matches that of the original triangular blocks. The updated densities of the gable blocks are denoted as "$\rho_{\mathrm{mG_i}}$," where "i" follows the naming scheme in Fig. 5. Second, the mass of the accelerometers attached to specimens is included in the numerical models by increasing the density of the neighboring blocks (see Fig. 3) as detailed in Eq. 1. Specifically, this regards the top block of the gable ($\rho_{\mathrm{mG_5}}$) in all numerical specimens, and the top corner blocks of the flanges, indicated with "ρ_{mF}," and the bottom right (East) corner of the main wall window, indicated with "ρ_{mW}," in tests 16, 17, 18, 19, and 23. Third, as the material characterization tests have been conducted on 1:15-scaled specimens, all input parameters extracted from their corresponding numerical models (also created for 1:15-scale specimens) are converted to full scale while preserving the Cauchy similitude (Harris and Sabnis 1999). Parameters with displacement dimensions ($\mathrm{u_k}$, δ_k, and δ_e with the mm unit) are upscaled by $\lambda_\mathrm{L}^{-1}=15$, those with contact stiffness dimensions ($\mathrm{k_{no}}$, $\mathrm{k_{nt}}$, $\mathrm{k_s}$ with the N/mm^3 unit) are downscaled by $\left(\lambda_\mathrm{E}\lambda_\mathrm{L}^{-1}\right)^{-1}=1/15$, and dimensionless parameters (ν_m and $\tan\phi$), densities (ρ_m, $\rho_{\mathrm{mG_{1-5}}}$, ρ_{mF}, and ρ_{mW}), and parameters with the dimension of stress ($\mathrm{E_m}$, $\mathrm{f_t}$, and c with the N/mm^2 unit) are kept unchanged (λ_ρ=λ_E=$\lambda_\sigma=1$).

$$
\begin{aligned}
&\rho_{\mathrm{mG_i}} = \frac{\text{Orgininal } \mathrm{V_{Gi}}}{\text{Simplified } \mathrm{V_{Gi}}}\rho_\mathrm{m} \qquad\qquad \text{where} \quad \mathrm{i} = 1 \sim 4,\\
&\rho_{\mathrm{mG_5}} = \frac{\text{Orgininal } \mathrm{V_{Gi}}}{\text{Simplified } \mathrm{V_{Gi}}}\rho_\mathrm{m} + \frac{\mathrm{m_{OOP}} + \mathrm{m_{IP}}}{\text{Simplified } \mathrm{V_{Gi}}}\lambda_\mathrm{L}^3,\\
&\rho_{\mathrm{mF}} = \rho_\mathrm{m} + \frac{\mathrm{m_{OOP}} + \mathrm{m_{IP}}}{\mathrm{V_F}}\lambda_\mathrm{L}^3,\\
&\rho_{\mathrm{mW}} = \rho + \frac{\mathrm{m_{IP}}}{\mathrm{V_W}}\lambda_\mathrm{L}^3
\end{aligned}
\tag{1}
$$

The final input parameters, obtained via the calibration and scaling procedure detailed above, are summarized in Table 2. The values in parentheses indicate the original parameter values from the 1:15-scale material simulations prior to conversion to full scale. At the end of the material characterization phase, numerical models of the PEER material tests were also scaled up to full scale and analyzed with the final parameters listed in Table 2. The results showed perfect match with the small-scale simulations, confirming the validity of the adopted approach for preserving the Cauchy similitude law under quasi-static loading conditions.

3.3 Dynamic loading signals

The simulation of the shake-table tests is carried out by first applying gravity, followed by one of the 29 dynamic loading signals used in the PEER campaign (see Table 1) to each specimen. However, to maintain the Cauchy similitude (Harris and Sabnis 1999) between the full-scale numerical specimens and the 1:15-scale experimental ones, modifications are introduced in both loading steps. Firstly, to ensure that the numerical specimens undergo the same self-weight-induced stresses as the experimental ones ($\lambda_\sigma=1$), the 9.81 m/s^2 gravitational acceleration is down-scaled by $\lambda_\mathrm{a}^{-1}=1/15$ to 0.654 m/s^2 during gravity loading. Secondly, the scaling applied to the intensity and spectral content of the dynamic loading signals during the physical tests (see Section 2.3) is reverted. Specifically, the amplitude of the acceleration time-histories recorded by the shake table sensor during the experiments is down-scaled by $\lambda_\mathrm{a}^{-1}=1/15$ to impose equivalent stress levels in the numerical models ($\lambda_\sigma=1$), while their data collection intervals (time data) are up-scaled by $\lambda_\mathrm{T}^{-1}=15$ to align their spectral content with the natural frequencies of the full-scale numerical models

($\lambda_f = 15$). After these adjustments, the dynamic loading signals are cropped to retain only their high-intensity portions, corresponding to the intervals containing 1–99% of the total energy content, thereby reducing the duration of the analyses. The large 1–99% energy content band is particularly preserved to avoid neglecting any pre-peak parts of the signals that could affect the behavior during significant motions, as well as any post-peak parts that could lead to collapse. The signals are applied to the one-third bottom part of the base, which is kinematically coupled to a reference point at its center of geometry that is fixed in all its degree of freedom (DoFs), except for the OOP direction of the main wall, to which the loading signals are applied, as shown with a dashed green arrow in Fig. 5a. Finally, the signals are processed using linear baseline correction and a third-order band-pass Butterworth filter with cutoff frequencies between 0.2 Hz and 70 Hz (3–1050 Hz in the 1:15 scale) to eliminate electrical noise introduced by the data acquisition system (Boore and Bommer 2005). It should be noted that in previous works of the authors (Ghezelbash et al. 2025a, b, 2026a, b), loading signals used in dynamic simulation of experimental responses are each processed using unique filtering parameters, so that the displacement produced by each signal matches the real displacement time history recorded at the same location from which the signal is collected during the physical test. However, since no displacement time history was provided in the data of the PEER contest, this study adopts a single set of settings for all signals. Nevertheless, these settings are purposefully selected to preserve the majority of the spectral content while ensuring that only noise is removed. The one-by-one illustration of the signals processed via the cropping and cleaning explained here is presented in Appendix next to that of their raw variations to enable easier comparison, along with a discussion of the effects of the applied processing on the characteristics of the signals. It should be noted that the influence of discrepancies in the characteristics of processed and raw signals on the response of the structures is investigated during the numerical simulations, as explained in Sect. 4.

3.4 Analysis procedure

The gravity loading step is performed using a nonlinear static analysis framework. The subsequent dynamic loading is carried out via the implicit Hilbert–Hughes–Taylor (HHT) direct integration time-history analysis (Hilber et al. 1977). As shown in Fig. 8a, the HHT parameters are set to $\alpha_{\mathrm{HHT}} = -0.05$, $\gamma_{\mathrm{N}} = 0.55$, and $\beta_{\mathrm{N}} = 0.275625$. Additionally, a small maximum allowable time-stepping increment is adopted, corresponding to the sampling rate used to post-process the readings from the experimental sensors, upscaled to full scale ($\mathrm{t} = 0.003125$ s). The previous works of the authors (Ghezelbash et al. 2025a, b, 2026a) have demonstrated that these settings effectively prevent significant numerical dissipation of kinetic energy ($\mathrm{t}/\mathrm{T} \leq 4\%$) and reduce the risk of numerical divergence during increments involving high geometric or mechanical nonlinearity. Furthermore, the use of the same (upscaled here) collection rate as the experimental sensors enables a direct, one-to-one comparison of the numerical outputs with the experimental recordings.

Rayleigh damping is introduced in the expanded blocks, half-blocks, lintels, and the base to govern dynamic energy dissipation. As shown in Fig. 8b, both mass- and stiffness-proportional terms are employed, as permitted by the implicit HHT solver, without introducing additional computational costs (unlike in explicit solvers). Modal analysis is performed at the beginning of the simulations, prior to gravity loading, to identify the natural deformation

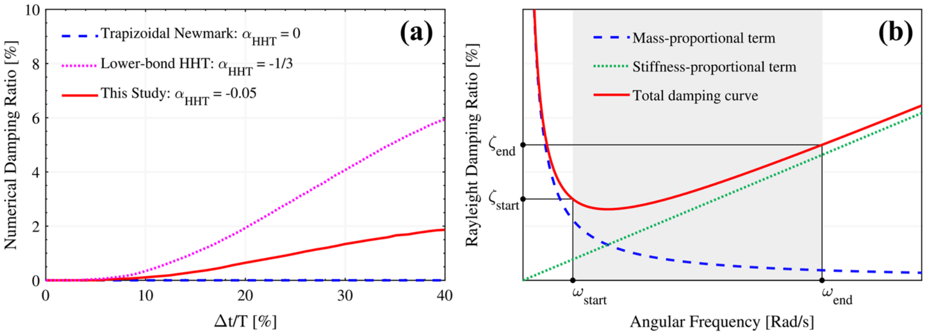

Fig. 8 Damping strategy adopted for dynamic simulations: numerical damping through the HHT implicit solver (**a**) and Rayleigh damping implemented in the blocks (**b**)

modes and their associated frequencies in the different numerical specimens with different instrumentation layouts. The natural frequencies are then used to calibrate the Rayleigh damping input parameters (α_R and β_R) assuming a target damping ratio of $\zeta_R = 5\%$ and $\zeta_{start} = \zeta_{end} = \zeta_R$. This target value is consistent with that found in the previous studies (Ghezelbash et al. 2025a, b, 2026a) of the authors to be suitable for simulating one- and two-way bending dynamic responses of unreinforced masonry under seismic loading. The calibration procedure for α_R and β_R based on the modal analysis results of the numerical specimens is further detailed in Sect. 5.1.

4 Accommodation of uncertainties related to modeling assumptions

The previous studies of the authors (Ghezelbash et al. 2025a, b) have highlighted the inherently chaotic nature of the dynamic responses in masonry structures and their high sensitivity to slight variations in structural properties, loading characteristics, and modeling assumptions. These observations underline the need for a statistical approach to the simulation of masonry dynamics to better account for the uncertainties influencing both experimental and numerical outcomes. In line with this objective, the batch of 29 simulations required for the blind-prediction contest is repeated multiple times within a parametric study, each series introducing variations in one or more modeling assumptions. The 23 variations considered for the parametric study are listed in Table 3 and are labeled “Vi”, with V0 representing the reference numerical models developed as described in Sect. 3. The parameters modified in each variation, compared to the V0 reference models, are highlighted in bold in the Table 3. Part of the variations considered here are intended to enable a targeted sensitivity analysis of the effects of the modeling assumptions (such as the filtering of the loading signals and damping) on the simulation outcomes, while the others, although not defined based on a probabilistic approach, are meant to accommodate the uncertainties in different (modal and material) properties of the tested specimens, as explained in more detail in the following.

During Phase 1, a total of 9 variations is considered to assess the influence of loading characteristics (V1), modal properties of the specimens (V2–3), material behaviors (V4–6), and damping (V7–8) on the structural response. The V1 variation applies the non-cleaned loading signals (i.e., signals obtained after cropping but before filtering and baseline cor-

Table 3 Different numerical variations considered for parametric study

Timeline	Variation	Dynamic Loading Signals	Block Stiffness	Joint Nonlinear Properties			Damping
			E_m [MPa]	f_t [MPa]	$\tan\phi$	u_k [mm]	ζ_R [%]
Phase 1	V0	Cleaned	7000 MPa	0.97 MPa	0.85	3.6 mm	5%
	V1	**Not Cleaned**[i]	7000 MPa	0.97 MPa	0.85	3.6 mm	5%
	V2	Cleaned	**14000 MPa**	0.97 MPa	0.85	3.6 mm	5%
	V3	Cleaned	**4500 MPa**	0.97 MPa	0.85	3.6 mm	5%
	V4	Cleaned	7000 MPa	**0.73 MPa**	0.85	3.6 mm	5%
	V5	Cleaned	7000 MPa	0.97 MPa	**0.64**	3.6 mm	5%
	V6	Cleaned	7000 MPa	0.97 MPa	0.85	**0.9 mm**	5%
	V7	Cleaned	7000 MPa	0.97 MPa	0.85	3.6 mm	**2.5%**
	V8	Cleaned	7000 MPa	**0.73 MPa**	0.85	3.6 mm	**2.5%**
Phase 2	V9	**Not Cleaned**	7000 MPa	0.97 MPa	0.85	3.6 mm	**2.5%**
	V10	Cleaned	**14000 MPa**	0.97 MPa	0.85	3.6 mm	**2.5%**
	V11	Cleaned	**4500 MPa**	0.97 MPa	0.85	3.6 mm	**2.5%**
	V12	Cleaned	7000 MPa	0.97 MPa	**0.64**	3.6 mm	**2.5%**
	V13	Cleaned	7000 MPa	0.97 MPa	0.85	**0.9 mm**	**2.5%**
	V14	Cleaned	7000 MPa	0.97 MPa	0.85	3.6 mm	**1.5%**
	V15	**Not Cleaned**	7000 MPa	0.97 MPa	0.85	3.6 mm	**1.5%**
	V16	Cleaned	**14000 MPa**	0.97 MPa	0.85	3.6 mm	**1.5%**
	V17	Cleaned	**4500 MPa**	0.97 MPa	0.85	3.6 mm	**1.5%**
	V18	Cleaned	7000 MPa	**0.73 MPa**	0.85	3.6 mm	**1.5%**
	V19	Cleaned	7000 MPa	0.97 MPa	**0.64**	3.6 mm	**1.5%**
	V20	Cleaned	7000 MPa	0.97 MPa	0.85	**0.9 mm**	**1.5%**
	V21	Cleaned	7000 MPa	0.97 MPa	0.85	3.6 mm	**1.5% – Wider Range**[ii]
	V22	Cleaned	7000 MPa	0.97 MPa	0.85	**0.9 mm**	**1.5% – Wider Range**

[i] Signals produced after cropping and before cleaning (baseline correction and filtering) are used for dynamic loading

[ii] A wide frequency range is used in damping calibration to under-damp the first ten natural modes

rection) to evaluate and potentially isolate the uncontrolled influence of signal processing on the dynamic responses. Variations V2 and V3 modify the elastic modulus of masonry (E_m) to 200 and 65% of the values used in the reference models, respectively, to explore the impact of stiffness variations on the amplification of dynamic effects. These values correspond to the upper and lower bounds of E_m fitted to the outcomes of PEER uniaxial compression tests performed on wallets (Del Giudice et al. 2024) in the numerical models (see Fig. 7). In variations V4 and V5, the tensile strength (f_t) and the friction coefficient ($\tan\phi$) of the joints are each reduced by 25%, consistent with the variation observed in the response of the PEER wall IP tests with (see Fig. 7). The friction coefficient is shown to have the most significant influence on the strength of the walls in IP characterization tests, and its reduction in the parametric study aims to capture the uncertainties inherent in property estimation from experimental data. Similarly, the property f_t, although having limited influence on the results of the IP simulations, is shown during preliminary dynamic analyses to play a significant role in the OOP response of the sub-structures. This is primarily due to the stabilization of the sub-structures relying solely on self-weight, which causes the masonry units to displace and fall even under minimal excitation if sufficient cohesive strength is not considered in the joints. Variation V6 significantly reduces the tensile softening length (u_k) in the joints by 75% as the OOP response of the sub-structures is expected to exhibit more brittle failure compared to the behavior observed in the wall IP experiments. Such a reduction also includes the consequences of the potential defects, not explicitly simulated in the numerical models, as they can substantially diminish the ductility of the specimens and promote a more brittle failure. The reduced value (0.6 mm in the original 1:15 scale) falls within the plausible range identified during material characterization simulations. It is also in line with the typical softening behavior observed in Calcium Silicate masonry units (Jafari 2021) and is deemed appropriate for producing brittle failures. Finally, variations V7 and V8 investigate the effect of damping on the wall response by reducing the Rayleigh damping ratio (ζ_R) in the blocks by 50% compared to the reference models. In V8, the tensile strength of the joints is also reduced by 25% to assess whether lower damping combined with weakened joints leads to a higher likelihood of collapse.

During Phase 2, a total of 14 additional variations (V9–22) are introduced based on comparisons between the modal response and damping characteristics of the numerical specimens and the experimental data published from dynamic identification tests. As discussed in detail in Sect. 5.1, the tested sub-structures exhibit natural frequencies that closely align with those of the numerical models but consistently show lower damping levels than the value (5%) originally assumed in the several numerical models of Phase 1 (V0–6). The implications of this discrepancy are thoroughly investigated in Phase 2. Variations V9–13 adopt the same 2.5% damping ratio used in V8–9 models to complement the results of Phase 1 and to assess the combined effects of reduced damping and modified material properties or loading assumptions on substructure response. The 2.5% damping aligns with the average damping calculated for the first ten modes identified from hammer test data. Variations V14–20 further extend this investigation by using an even lower damping ratio (reduced by 70% to $\zeta_R = 1.5\%$) to represent extreme-scenario counterparts of the V0–6 models. The 1.5% damping ratio is chosen based on the damping calculated for the first mode of vibration extracted from hammer test data. Since the hammer tests are conducted on specimens in operational conditions, the 1.5% damping ratio is considered a lower-bound estimate of the damping likely to be present in near-collapse regimes. Additionally, variation V21 introduces an even more extreme case in which a broader frequency range is used for Rayleigh damping calibration, resulting in underdamping ($\zeta < 1.5\%$) in the first ten natural modes of the specimens. In variation V22, these conditions are combined with a brittle post-peak response in the joints (u_k reduced by 75%), representing an extreme case that is expected to allow the identification of more potential collapses. It should be noted that for variations V2, V3, and V7–22, the Rayleigh damping parameters are recalculated to reflect the updated stiffness of the structure due to the changes applied.

5 Simulation results and discussion

This section presents the outcomes of the analyses conducted on the numerical models developed as described in Sects. 3 and 4. The results of the modal analyses for the different model variations are first presented and compared against experimental observations. Afterwards, the results of the dynamic analyses are reported in terms of probability of collapse, observed failure mechanisms, and maximum OOP displacements recorded for all the conducted simulations, in accordance with the requirements of the blind-prediction contest. It should be noted that the experimentally recorded modal information presented in this section was only made available after the conclusion of the Phase 1 of the blind-prediction contest. In this section, the real outcomes of the 29 experiments are not discussed to keep focus on the activities of the authors during the blind-prediction contest. Only the video of the proof-of-concept shake table experiment, published by the organizers along with the Phase 1 data, is referenced in various parts of this section to illustrate the rationale by which the authors evaluated their results before submission of a response to the blind-prediction contest and before the real experimental outcomes were released.

5.1 Modal analysis

The frequencies of the first ten natural vibration modes for the different numerical model variations and instrumentation layouts are listed in Table 4. To validate the back-scaling procedure adopted in this study, modal analyses are conducted on both the full-scale numerical models used in the dynamic analyses and their corresponding 1:15-scale counterparts. The full-scale and scaled models exhibit similar deformation modes, and their natural frequencies satisfy the expected proportionality with the scaling factor $\lambda_f^{-1} = 1/15$, in accordance with Cauchy similitude in the dynamic regime (Harris and Sabnis 1999). Only the frequencies of the 1:15-scale numerical models are listed in Table 4 to facilitate direct comparison with the experimental data. In terms of instrumentation layout, specimens from tests 16, 17, 18, 19, and 23 in each variation exhibit less than 2% difference in natural frequencies compared to other specimens across all natural modes. Similarly, the specimens with the dynamic test instrumentation layout show very similar frequencies to those with the ham-

Table 4 Frequencies (in Hz) associated with natural modes of vibration of numerical specimens

Mode #	Modal Identification Instrumentation[i]			Typical Dynamic Loading Instrumentation[ii]			Refined Dynamic Loading Instrumentation[iii]		
	All Vars.	V2/9/15 Var.	V3/10/16 Var.	All Vars.	V2/9/15 Var.	V3/10/16 Var.	All Vars.	V2/9/15 Var.	V3/10/16 Var.
	(Reference)	($2E_m$)	($0.65E_m$)	(Reference)	($2E_m$)	($0.65E_m$)	(Reference)	($2E_m$)	($0.65E_m$)
1	180.9	204.6	163.1	184.3	208.4	166.3	178.5	202.0	160.9
2	195.1	219.0	176.7	198.4	222.7	179.7	192.8	216.5	174.6
3	223.7	248.6	204.3	225.7	250.9	206.1	222.4	247.2	203.2
4	415.2	451.6	385.2	416.5	453.0	386.5	414.0	450.4	384.1
5	431.6	472.1	398.5	435.6	476.5	402.2	428.9	469.2	396.1
6	492.8	543.8	452.3	498.3	549.5	457.5	489.4	540.1	449.1
7	562.3	607.7	524.1	565.3	611.1	526.8	560.1	605.2	522.1
8	644.5	706.0	595.5	648.1	710.0	598.7	641.5	702.8	592.7
9	709.7	779.4	647.6	712.3	784.3	649.3	706.7	775.8	644.8
10	746.5	819.1	693.8	750.8	822.0	698.3	741.2	813.4	689.2

[i] Shown in Fig. 4b used during hammer tests

[ii] Shown in Fig. 3 and used in all tests

[iii] Shown in Fig. 3 and used in tests 16, 17, 18, 19, and 23

mer test instrumentation layout. This indicates that the additional mass and the layout of the instruments have a negligible influence on the modal behavior of the sub-structures.

The modal shapes associated with the natural modes of vibration of numerical specimens configured with the hammer test instrumentation layout (Fig. 4b) are illustrated in Fig. 9a. The corresponding modal frequencies and participating masses for each mode are presented in Fig. 9b and c, respectively. The data for the V0 reference models and variations with the original block stiffness (E_m) are shown with a solid blue line with circle markers, while the results for the V2/9/15 (higher E_m) and V3/10/16 (lower E_m) variations are represented with a green dashed line with square markers and a red dashed-dotted line with triangle markers, respectively. According to Fig. 9a, the first and second deformation modes extracted from the numerical models correspond to OOP deformation of the opening and the solid flange in the East-West direction (along x-axis), respectively. This observation aligns particularly well with the collapse mechanism observed in the proof-of-concept specimen tested prior to the 29 shake table experiments. In that test, failure occurred through the OOP collapse of the opening flange. The third and fourth modes are associated with OOP deformations of the main wall in the North-South direction (along z-axis), with the third mode displaying a single-curvature pattern and the fourth mode exhibiting a double-curvature behavior. The fifth mode corresponds to a double-curvature OOP deformation of the flanges. The sixth mode and above are characterized by more complex deformation shapes, with the seventh

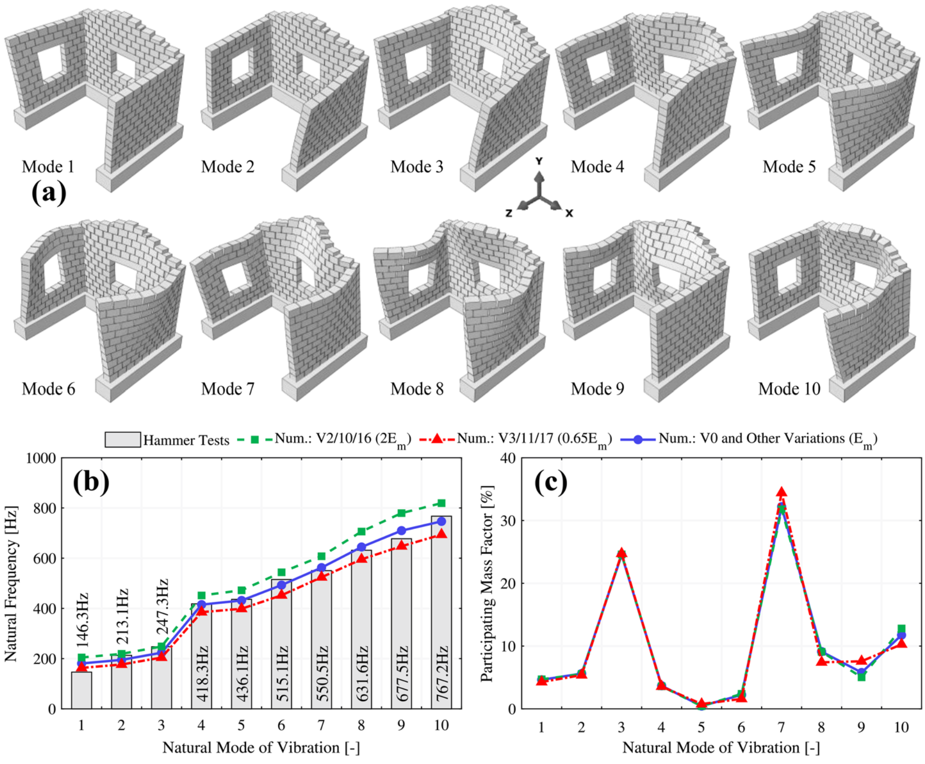

Fig. 9 Modal analysis results for the numerical specimens: modal shapes (**a**), frequencies (**b**), and participating mass factors (**c**) of the first ten natural modes of vibration across different variations of the models. The deformed shapes are scaled with different factors for clear visualization

mode exhibiting the highest participating mass across all modes and model variations, as shown in Fig. 9c. It should be noted that variations in the elastic properties or the instrumentation layout do not influence the deformed shapes or the sequence of their appearance in the natural vibration modes. However, changes in the Elasticity Modulus of the blocks (E_m) lead to frequency shifts of up to 14% and minor changes in the participating masses in the eighth to tenth deformation modes, as shown in Fig. 9b and c, respectively. However, such differences are significantly smaller than the variations considered for the parameter (100% higher in V2/9/15 and 35% lower in V3/10/16).

The modal features of the tested sub-structures are extracted by the authors from hammer test data published during Phase 2 using the methodologies outlined in (Ewins 2000) and are listed in Table 5. The frequencies of the numerical model with the reference material properties and the hammer-test sensor layout show good agreement with those extracted from the hammer test data, illustrated with gray bars in Fig. 9b. Differences between experimental and numerical frequencies remain within 5% in the fourth and higher modes, increase to 10% for the second and third modes, and reach 24% for the first mode. These discrepancies do not follow a consistent trend: the first-mode experimental frequency is lower than that of the V0 numerical specimens and aligns more closely with the V2/9/15 variations, whereas the experimental frequencies of the second and third modes are higher than those of the V0 model and better match the results of the V3/10/16 variations. As highlighted in bold in Table 5, satisfactory MAC values between numerical and experimental modal shapes (above 0.8 and not below 0.4, as established in (Gentile and Saisi 2007; Aşıkoğlu et al. 2019)) are observed across all modes with the lowest value being 0.65 in the seventh mode. It should be noted that, while the difference between the numerical and experimental first-mode frequencies is significant, no further adjustment of the numerical specimens is considered in order to keep the study consistent. Moreover, since variations with better-matching frequencies (V2/9/15 and V3/10/16) are already considered in the study, the potential consequences of the mismatch between the modal behavior of the numerical and experimental specimens are assumed to have already been accommodated.

For Rayleigh damping calibration in the numerical models, the first and third natural frequencies of the full-scale numerical models (equal to the frequencies of Table 4 multiplied by $\lambda_f^{-1} = 1/15$) are used consistently across all numerical variations. For each specimen, the frequencies extracted using the instrumentation layout in its corresponding test are used. The first and third modes are specifically selected because they already include all deformation patterns deemed to have appeared during the tests and the collapse of the specimens (as observed in the proof-of-concept video), as well as because the higher modes correspond to double- and triple-curvature deformations with lower importance. Particularly, the first mode is selected due to its expected prominence during the shake table tests (as shown in the case-study video), while the third mode is chosen because of its association with the OOP deformation of the main wall, characterized by a large participating mass and a substantial influence on the overall dynamic response. Higher-order modes, particularly the seventh, are deemed unlikely to dominate the response because of their high frequencies (400 Hz and above), at which the spectral intensity of the loading signals is very low. However, the potential influence of these modes is investigated in the V20 models, wherein the frequencies of the first and tenth natural deformation modes are used to calibrate the Rayleigh damping parameters. It should be noted that the damping ratios extracted from Phase 2 hammer test data are significantly lower than the 5% assumed during Phase 1, with 1.6%

Table 5 Data extracted from Phase 2 identification tests of experimental sub-structures

Mode	Frequency	Modal Assurance Criterion (MAC) Calculated Against Deformation Modes of Numerical Models[i]										Damping
		Mode 1	Mode 2	Mode 3	Mode 4	Mode 5	Mode 6	Mode 7	Mode 8	Mode 9	Mode 10	
Mode 1	146.3	**0.92**	0.38	0.50	0.16	0.39	0.63	0.22	0.68	0.61	0.27	1.6%
Mode 2	213.1	0.40	**0.95**	0.91	0.47	0.75	0.90	0.38	0.80	0.44	0.55	4.2%
Mode 3	247.3	0.18	0.81	**0.83**	0.55	0.64	0.70	0.48	0.70	0.40	0.65	3.7%
Mode 4	418.3	0.17	0.58	0.80	**0.70**	0.46	0.55	0.70	0.65	0.63	0.75	1.0%
Mode 5	436.1	0.45	0.80	0.50	0.39	**0.99**	0.88	0.29	0.85	0.14	0.26	9.1%
Mode 6	515.1	0.81	0.67	0.59	0.28	0.76	**0.88**	0.28	0.91	0.40	0.30	2.2%
Mode 7	550.5	0.21	0.40	0.42	0.62	0.53	0.56	**0.65**	0.58	0.41	0.70	1.1%
Mode 8	631.6	0.46	0.72	0.88	0.52	0.61	0.78	0.54	**0.85**	0.69	0.67	1.9%
Mode 9	677.5	0.48	0.71	0.97	0.38	0.43	0.73	0.38	0.69	**0.79**	0.66	1.2%
Mode 10	767.2	0.21	0.40	0.42	0.62	0.53	0.56	0.65	0.58	0.41	**0.70**	1.4%

Results from the numerical model with the reference material properties and the hammer test instrumentation layout are used damping observed for the first vibration mode and an average of 2.7% across all modes. The effect of these differences is also investigated in the V7-20 simulations. It should also be noted that the largest first-mode frequency observed across the numerical specimens results in $t/T = 0.4\%$, which in turn leads to negligible numerical damping in the numerical simulations. This means that the response of the numerical specimens has been primarily governed by Rayleigh damping.

5.2 Probability of collapse

The peak OOP displacements, measured relative to the base and recorded at the top of the gables in the numerical specimens, are presented in the heatmap in Fig. 10. The same control point used in the experiments is adopted for data collection. For consistency and ease of comparison with the experimental outcomes, the numerical displacement values, obtained from 1:1-scale specimens, are downscaled by $\lambda_L^{-1} = 1/15$ to the 1:15 scale of the tested substructures. Most numerical specimens remain stable under dynamic loading, exhibiting neither discernible damage nor significant deformation. However, five specimens, specifically those corresponding to tests 11, 12, 13, 14, and 28 (House_11, House_12, House_13, House_14, and House_31), exhibit large OOP displacements relative to the wall thickness (denoted by "t" in the figure). In some variations, indicated with gray crosses in Fig. 10, these specimens also show collapse in the form of falling portions of the substructures and numerical divergence due to the inability of the remaining parts to return to equilibrium.

Given the occurrence of the large displacements reported in Fig. 10, a classification criterion is introduced to identify simulations that may indicate potential failure in addition to those showing explicit collapse. Prior studies by the authors on one- and two-way bending OOP responses (Ghezelbash et al. 2025, 2026) suggest that displacements exceeding 20% of wall thickness may compromise the dynamic stability of masonry walls, particularly those with height-to-thickness slenderness ratios similar to the main wall in this study ($h/t = 12.8$). Conversely, the deformation patterns observed in the numerical specimens, examples of which are shown in Fig. 11, indicate that significant cracking of the sub-structures, highlighted with dotted circles in the figure, initiates only when peak OOP displacements reach almost 30% of wall thickness. Conservatively, simulations showing OOP displacements greater than the average of these two thresholds (25% of wall thickness) are considered potential indicators of failure in the corresponding experiments. As highlighted in red in the heatmap of Fig. 10, a total of six specimens are identified using this criterion. Five of these correspond to tests 11, 12, 13, 14, and 28 (House_11, House_12, House_13, House_14, and House_31), already identified as susceptible to collapse by showing clear failure in some analyses. Among them, the specimen from test 11 (House_11) consistently exhibits OOP displacements exceeding the threshold across all numerical variations, while those from tests 12, 13, 14, and 28 (House_12, House_13, House_14, and House_31) exceed this threshold primarily in variations with reduced damping ratios ($\zeta_R \leq 2.5\%$ in V7–22). The remaining specimens show relatively small displacements, and only one additional specimen, from test 24 (House_27), is identified through this criterion, exceeding the 25% threshold in a few simulations. However, this specimen shows peak OOP displacements only marginally above the threshold and no significant cracking. Therefore, the original five specimens showing both clear failure in some simulations and large OOP displacements in the others are identified as those most likely to have experienced collapse during the experi-

Simulation Number and Specimen Name	Phase 1 (Before Having Hammer Test Data)									Phase 2 (After Having Hammer Test Data)													
	V0 (Reference)	V1 (Raw Signals)	V2 ($2E_m$)	V3 ($0.65E_m$)	V4 ($0.75f_t$)	V5 ($0.75\tan\phi$)	V6 ($0.25u_k$)	V7 ($0.5\zeta_R$)	V8 ($0.5\zeta_R$, $0.75f_t$)	V9 ($0.5\zeta_R$, Raw Sig.)	V10 ($0.5\zeta_R$, $2E_m$)	V11 ($0.5\zeta_R$, $0.65E_m$)	V12 ($0.5\zeta_R$, $0.75\tan\phi$)	V13 ($0.5\zeta_R$, $0.25u_k$)	V14 ($0.3\zeta_R$)	V15 ($0.3\zeta_R$, Raw Sig.)	V16 ($0.3\zeta_R$, $2E_m$)	V17 ($0.3\zeta_R$, $0.65E_m$)	V18 ($0.3\zeta_R$, $0.75f_t$)	V19 ($0.3\zeta_R$, $0.75\tan\phi$)	V20 ($0.3\zeta_R$, $0.25u_k$)	V21 ($0.3\zeta_R$, Wider Damping Range)	V22 ($0.3\zeta_R$, Wide. Damp. Ran., $0.25u_k$)
#1 (House_1)	0.89	0.87	0.70	1.40	0.90	0.93	0.90	1.00	1.07	1.00	0.76	1.65	1.50	1.11	1.68	1.61	0.92	1.56	1.75	1.68	1.64	1.43	1.57
#2 (House_2)	0.54	0.53	0.39	0.60	0.54	0.53	0.54	0.61	0.61	0.61	0.52	0.68	0.57	0.61	0.56	0.60	0.64	0.76	0.56	0.67	0.56	0.61	1.07
#3 (House_3)	0.69	0.69	0.71	0.81	0.69	0.72	0.69	0.98	1.01	0.92	0.76	0.97	1.04	1.00	1.09	1.00	0.75	1.00	1.07	1.10	1.08	1.07	1.07
#4 (House_4)	0.28	0.30	0.29	0.41	0.28	0.29	0.29	0.38	0.38	0.38	0.39	0.61	0.42	0.38	0.52	0.56	0.40	0.77	0.52	0.60	0.54	0.43	0.44
#5 (House_5)	0.99	3.65	0.68	1.11	0.95	1.00	1.00	1.08	1.11	1.07	0.81	1.21	1.16	1.10	1.19	1.19	0.89	1.25	1.19	1.21	1.21	1.12	1.15
#6 (House_6)	0.40	0.39	0.37	0.46	0.40	0.42	0.40	0.50	0.50	0.48	0.43	0.51	0.51	0.50	0.53	0.52	0.53	0.57	0.53	0.53	0.53	0.51	0.51
#7 (House_7)	0.39	0.38	0.32	0.43	0.39	0.41	0.39	0.40	0.40	0.39	0.33	0.50	0.41	0.40	0.40	0.40	0.34	0.55	0.40	0.42	0.40	0.40	0.40
#8 (House_8)	1.51	1.56	1.20	1.87	1.69	1.72	1.62	2.36	2.38	2.39	1.58	2.46	2.39	2.38	2.64	2.62	2.51	2.92	2.67	2.64	2.63	2.47	2.46
#9 (House_9)	0.49	0.48	0.55	0.59	0.49	0.49	0.49	0.55	0.55	0.53	0.60	0.76	0.57	0.56	0.66	0.57	0.65	0.90	0.66	0.66	0.66	0.59	0.60
#10 (House_10)	0.85	0.79	0.68	0.96	0.86	0.87	0.85	0.95	0.97	0.91	0.80	0.96	0.96	0.96	1.00	0.97	0.81	0.97	1.02	1.00	1.00	0.97	0.98
#11 (House_11)	4.28	4.23	3.31	5.05	4.80	4.63	5.83	8.12	5.78	6.96	5.66	6.23	6.46	16.80	7.62	6.90	7.24	7.73	7.43	7.42	8.42	6.98	12.42
#12 (House_12)	2.03	2.00	1.73	2.44	1.77	2.27	2.13	3.27	4.24	3.34	3.08	3.92	3.54	4.57	4.25	4.35	4.08	4.06	4.24	4.46	9.26	3.61	5.59
#13 (House_13)	1.26	1.29	1.12	2.51	1.44	1.29	1.26	1.55	2.70	1.58	1.35	2.53	1.96	1.89	2.61	2.48	1.40	6.16	2.85	8.50	2.88	2.03	2.37
#14 (House_14)	2.35	2.29	1.97	3.53	2.46	2.71	2.49	4.12	4.84	3.82	2.33	4.72	4.69	4.18	4.60	4.78	2.61	6.00	6.48	6.52	17.23	4.26	4.79
#15 (House_15)	1.57	1.56	1.56	1.64	1.48	1.57	1.57	1.66	1.57	1.67	1.59	2.16	1.67	0.74	1.70	1.72	1.61	2.20	1.59	1.70	1.67	1.68	1.66
#16 (House_17)	0.27	0.26	0.28	0.30	0.27	0.28	0.27	0.29	0.29	0.26	0.28	0.34	0.30	0.29	0.32	0.31	0.30	0.29	0.30	0.35	0.32	0.29	0.29
#17 (House_18)	0.42	0.43	0.30	0.54	0.42	0.43	0.42	0.49	0.49	0.31	0.30	0.59	0.51	0.49	0.55	0.56	0.38	0.62	0.55	0.35	0.37	0.53	0.34
#18 (House_19)	0.45	0.45	0.42	0.28	0.45	0.46	0.45	0.51	0.51	0.51	0.36	0.60	0.52	0.51	0.64	0.64	0.42	0.68	0.64	0.68	0.33	0.57	0.57
#19 (House_20)	0.55	0.54	0.45	0.63	0.55	0.56	0.55	0.60	0.60	0.57	0.49	0.64	0.62	0.61	0.62	0.62	0.55	0.71	0.62	0.68	0.63	0.62	0.59
#20 (House_21)	0.44	0.44	0.37	0.54	0.44	0.43	0.44	0.43	0.43	0.44	0.38	0.51	0.42	0.43	0.44	0.44	0.38	0.62	0.44	0.43	0.44	0.44	0.44
#21 (House_22)	0.35	0.37	0.37	0.47	0.39	0.29	0.29	0.39	0.33	0.33	0.39	0.61	0.33	0.33	0.41	0.41	0.33	0.33	0.30	0.28	0.26	0.32	0.32
#22 (House_23)	0.39	0.40	0.36	0.46	1.36	0.40	0.39	0.51	0.51	0.51	0.43	0.55	0.57	0.52	0.64	0.64	0.47	0.61	0.64	0.62	0.64	0.59	0.59
#23 (House_24)	1.36	1.36	1.14	1.37	1.47	1.38	1.37	1.79	1.69	1.80	1.38	1.67	1.70	1.79	1.94	1.94	1.76	1.73	1.69	1.71	1.87	1.85	1.82
#24 (House_27)	1.23	1.24	0.99	3.08	0.75	1.74	1.34	2.28	2.77	2.33	0.84	3.47	3.43	2.46	2.84	2.68	2.80	3.47	3.87	4.14	3.97	2.84	3.10
#25 (House_28)	0.74	0.66	0.79	1.23	0.75	0.79	0.75	0.85	1.04	0.85	0.76	2.11	1.05	0.97	1.15	1.22	0.75	2.37	1.94	2.29	2.38	1.02	1.11
#26 (House_29)	1.22	1.21	1.07	1.74	1.34	1.31	1.27	1.46	1.66	1.41	0.99	1.74	1.73	1.51	1.76	1.72	1.04	1.66	1.92	1.86	1.77	1.65	1.68
#27 (House_30)	1.48	1.44	1.29	1.59	1.56	1.49	1.48	1.62	1.78	1.51	1.49	1.95	1.70	1.67	1.81	1.67	1.53	2.89	2.10	2.11	2.03	1.68	1.80
#28 (House_31)	3.40	3.48	3.22	3.93	3.63	3.59	3.75	4.68	6.13	4.52	3.98	5.01	4.25	8.10	5.91	5.57	4.52	11.47	10.80	7.76	13.05	2.95	5.93
#29 (House_32)	1.18	1.16	0.94	1.25	1.19	1.20	1.19	1.18	1.09	1.34	1.05	1.37	1.37	1.16	1.06	0.88	1.11	1.24	1.12	1.27	1.09	1.13	1.11

Numerical Model Variation

0.6t 0.5t 0.4t 0.3t 0.2t 0.1t 0.0t

Fig. 10 Peak OOP displacements of the top of the gable predicted by different variations of the numerical models. The values of the displacements are shown in each cell in mm. Displacements exceeding 25% of the wall thickness (indicated with "t" in the legend) are highlighted with progressively darker shades of red as the amount of displacement increases. The simulations showing collapse are highlighted with gray cross marks

ments. It should be noted that collapses in these specimens typically occur when the peak OOP displacement of the gable approaches 60% of wall thickness. Hence, the upper-bound of the heatmap in Fig. 10 is limited to 0.6t.

Further analysis of the data presented in Fig. 10 reveals two insights regarding the numerical models. First, peak OOP displacements in tests 12, 13, 14, and 28 (House_12, House_13, House_14, and House_31) become significant only in the lower-damping variations, which suggests that the original 5% damping assumed in the Phase 1 analyses may have over-damped the response, thereby suppressing the realistic development of wall deformations and associated damage. Second, the occurrence of collapse predominantly in simulations adopting more brittle material properties (V13, V20, and V22) is consistent with the brittle

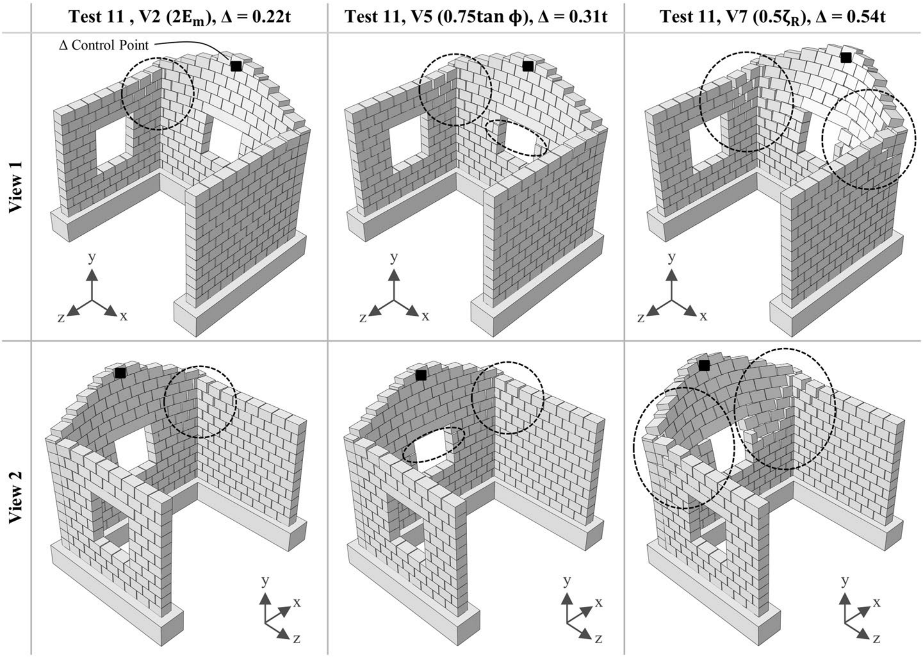

Fig. 11 Deformed shapes and damage patterns of numerical specimens with different levels of maximum OOP displacements: variations V2 (**a**), V5 (**b**), and V7 (**c**) of the specimen under test 11, under peak gable OOP displacements (Δ) equal to 22, 31, and 54% of thickness respectively. Deformed shapes are magnified with different factors for clear visualization. The dashed circles highlight the regions where the significant cracks form

OOP behavior captured in the proof-of-concept video and supports the hypothesis of the authors that the OOP response of the sub-structures may have been more brittle than the IP response of the walls. This hypothesis is further substantiated by the absence of collapse in other simulations, such as those for test 11 (House_11) using lower damping (V7 and V14) and reduced material strengths (V18 and V19). In these variations, the likely overestimation of softening behavior inhibits the free movement of the gables, despite the development of multiple cracks and the expected complete degradation of joint strengths. Instead, the large softening length maintains unrealistically high cohesive forces within the cracked regions, ultimately preventing full detachment and collapse of the gables.

5.3 Failure mechanisms

The types of failure mechanisms and damage patterns observed across various numerical simulations, both those that resulted in collapse and those exhibiting only large deformations without collapse, are summarized in Table 6 and illustrated in Fig. 12. The damage patterns follow an “X–Y” naming scheme. The first component, “X,” denotes the direction of peak OOP displacement of the gables: either towards the flanges (Inward Deformation, or ID), or away from them (Outward Deformation, or OD). The second component, “Y,” identifies the damage type, which includes cracking at the wall–flange connections (Corner Cracking, or CC), cracking at the lintel corners in the opening flange (Lintel Cracking, or

LC), rocking of the opening flange in its plane (Flange Rocking, or FR), OOP rocking of the gable (Gable Rocking, or GR), detachment of the main wall from the flanges at wall-flange connections (Corner Failure, or CF), and various forms of failure in the gables (Gable Failure, or GF). It should be noted that the V8 variation is placed between V11 and V12 models for easier comparison of the columns under each damping ratio class. Moreover, damage patterns in simulations with 5% damping (V1–6) are excluded from Table 6, as they are less frequent and closely resemble those already presented.

ID: Inward Displacement, OD: Outward Displacement, CC: Corner Cracking, LC: Lintel Cracking, FR: Flange Rocking, GR: Gable Rocking, CF: Corner Failure, GF: Gable Failure

The failure mechanisms of the simulations showing collapse, highlighted in bold in Table 6 and belonging to numerical specimens of tests 11, 12, 13, 14, and 28 (House_11, House_12, House_13, House_14, and House_31), are primarily governed by the OOP movement of the gable and its overturning or severe cracking. In V13 and V22 variations of Test 14 (House_14), however, the failure involves the falling of the lintel of the flange, resulting in numerical divergence before a complete cracking pattern develops. In the V14 models (with reduced damping), more pronounced cracking is observed at the connection between the main wall and the opening flange, particularly in tests 11 and 28 (House_11 and House_31). The damage patterns of the remaining simulations reveal two key findings. First, the crack patterns observed in simulations with varying damping ratios are generally consistent, though minor differences arise, such as more pronounced cracking at lintel corners and flange rocking in the less-damped simulations. Second, while the deformation patterns are generally similar, the direction of the peak OOP displacement varies due to the inherent randomness of dynamic behavior. Despite appearing minor, this variation significantly influences the explicit identification of collapse outcomes. For instance, in the V17 variation of test 28 (House_31), although a substantial deformation is recorded (76% of wall thickness), the gable does not collapse during the simulation. This is because, instead of deforming outward, the gable moves inward, which in turn inhibits failure due to the asymmetricity of the specimens and their greater resistance to inward movement. Thirdly, a comparison of the V20 simulations for tests 12 and 24 (House_12 and House_27) reveals the role of loading characteristics. Despite being loaded with ground motions of similar magnitude, House_27 shows the gable moving toward the flanges, thereby preventing collapse, whereas House_12 shows outward movement of the gable.

The failure mechanisms and damage patterns in the numerical are consistent with findings from both experimental and numerical studies on masonry sub-structures with similar geometrical configurations subjected to dynamic loading (Candeias et al. 2016b; Canditone et al. 2025), thereby supporting the reliability of the present results. However, given the limited number of collapsing specimens, a comprehensive investigation into the record-to-record variability of collapse mechanisms across all 29 cases could not be carried out.

5.4 Displacement demands

The distribution of peak gable OOP displacements observed across all variations of each sub-structure specimen is shown in the box plots of Fig. 13. Each box plot represents the range of displacement data, including the minimum, 16th percentile, median, 84th percentile, and maximum values. The average (Avg) and standard deviation (StDv) for each numerical specimen are provided adjacent to the corresponding box. For visual clarity, the

Table 6 Types of failure mechanisms and crack patterns in numerical specimens showing conceivable damage

Specimen	Numerical Model Variations with Peak OOP Displacements Above 25% of Wall Thickness[i]															
	$\zeta_R = 2.5\%$							$\zeta_R = 1.5\%$							$\zeta_R = 1.5\%$ (Wide. Damp. Ran.)	
	V7	V9	V10	V11	V8	V12	V13	V14	V15	V16	V17	V18	V19	V20	V21	V22
	(Ref. Mat.)	(Raw Sign.)	$(2E_m)$	$(0.65E_m)$	$(0.75f_t)$	$(0.75\tan\phi)$	$(0.25u_k)$	(Ref. Mat.)	(Raw Sign.)	$(2E_m)$	$(0.65E_m)$	$(0.75f_t)$	$(0.75\tan\phi)$	$(0.25u_k)$	(Ref. Mat.)	$(0.25u_k)$
House_11	OD+GC[ii]	OD+GC	OD+CC	ID+CC	ID+CC	**OD+GF1**	**OD+CF**	OD+GC	OD+CC	ID+CC	ID+CC	ID+CC	**OD+GF1**	**OD+GF2**	**OD+GF1**	**OD+GF2**
House_12	–[iii]	–	–	ID+LC	OD+CC	–	OD+GR	ID+CC	ID+LC	ID+LC	ID+FR	ID+LC	OD+CC	**OD+GF3**	–	**OD+GF4**
House_13	–	–	–	–	–	–	–	–	–	–	ID–CC	–	**OD+GF5**	–	–	–
House_14	ID+LC	OD+LC	–	OD+LC	ID+LC	OD+CC	**ID+LF**	OD+LC	OD+LC	–	ID+LC	ID+LC	ID+CC	**OD+GF6**	OD+LC	**ID+LF**
House_27	–	–	–	–	–	–	–	–	–	–	–	–	OD+GC	OD+GR	–	–
House_31	ID+LC	OD+CC	–	OD+LC	ID+CC	ID+CC	**OD+GF7**	ID+CC	OD+CC	OD+CC	ID+CC	ID+LC	ID+LC	**OD+GF8**	–	**OD+GF9**

[i] The V1-6 variations are excluded here as their collapse is less frequent and their damage pattern resembles already presented

[ii] Different types of damage patterns are visualized in Fig. 12

[iii] These simulations do not show significant damage, and their peak OOP displacements are generally below the 25% threshold

ID: Inward Displacement, OD: Outward Displacement, CC: Corner Cracking, LC: Lintel Cracking, FR: Flange Rocking, GR: Gable Rocking, CF: Corner Failure, GF: Gable Failure

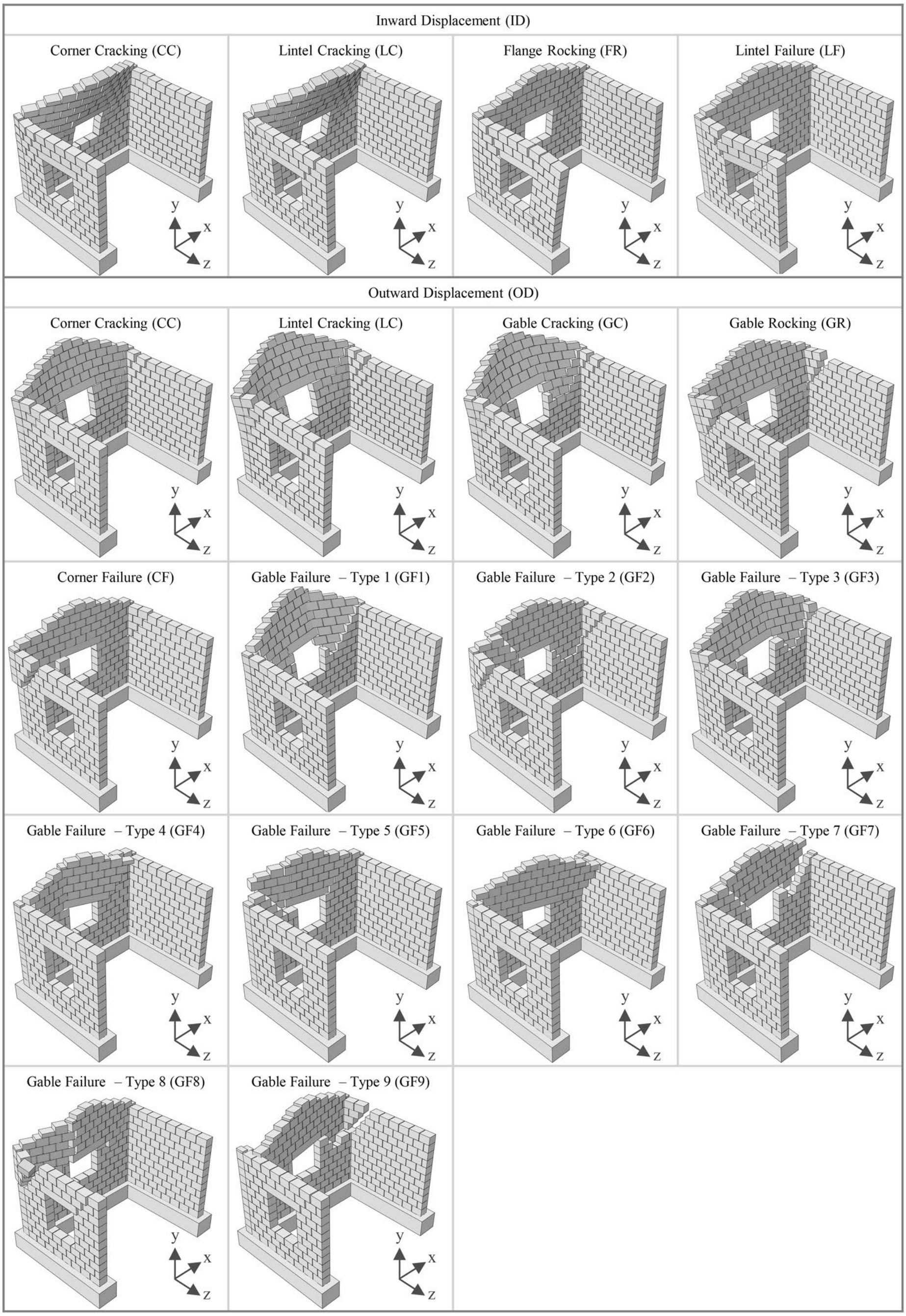

Fig. 12 Visualization of failure mechanisms observed during dynamic analyses. Deformed shapes are captured at the moment corresponding to the occurrence of peak OOP deformation at the top of the gables. Different magnification scales are used for each deformed shape for clear visualization

peak OOP displacements of collapsed specimens are capped at 60% of the wall thickness, with collapse events indicated by red crosses (×). Additionally, the peak loading intensity of each specimen, defined as the Peak Signal Acceleration (PSA) of the applied ground motion, is indicated with a green square marker. Several key observations can be drawn from Fig. 13. First, the predicted displacements demonstrate minimal scatter across most specimens, despite the inclusion of multiple variations in the numerical models. This suggests a high degree of consistency in the predictions for 24 out of the 29 tests. Significant scatter is observed only for the five specimens that experienced collapse. Second, greater variability emerges when specimens transition from elastic to nonlinear behavior, as cracking begins. For instance, the specimen from test 5 (House_5) exhibits consistent displacements across all variations, remaining below 10% of wall thickness, except in Variation V1, where displacements increase sharply once a 20% threshold is crossed. Similarly, tests 8, 23, 24, and 25 (House_8, House_24, House_27, and House_28) show slightly more scatter, as their OOP displacements are closer 20% of the wall thickness, underscoring the inherent chaos of dynamic responses once nonlinearities are introduced. Third, no clear correlation is found between peak loading intensity and resulting OOP displacement. For example, tests 27 to 29 are conducted under similar loading PSAs, yet the specimen of test 28 shows much larger OOP displacements. These findings demonstrate that dynamic structural responses are not governed solely by loading intensity; they are also strongly influenced by other excitation characteristics, such as the spectral content. This highlights the critical role of record-to-record variability and the limitations of using accelerations (such as PGA or, in this case, PSA) as an intensity measure for defining fragility curves within the seismic assessment framework. Indeed, several studies have explored the development of more representative intensity measures for selecting and classifying loading signals for experimental and numerical research (Caicedo et al. 2024a, b, 2025a). It should be noted that the observation presented here is purely based on the results of the numerical simulation. Such discrepancies may differ from those observed in the real world. Hence, additional validation of record-to-record variability through physical experiments is necessary.

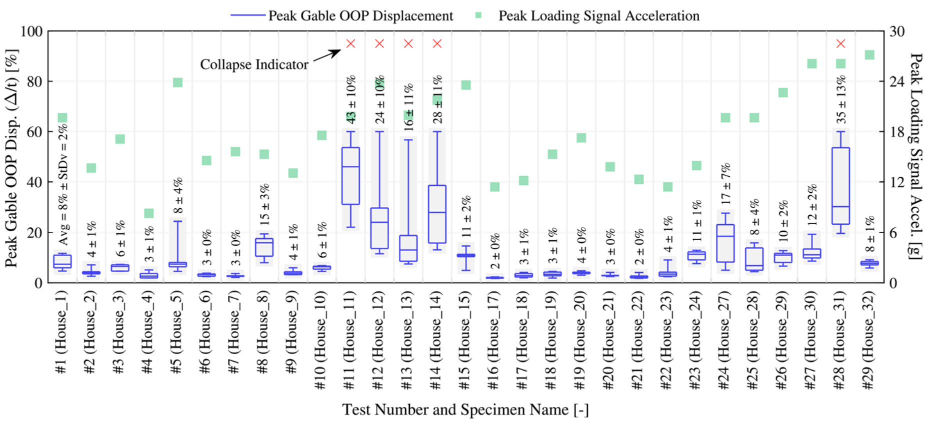

Fig. 13 Distribution of peak OOP displacements collected from different variations of the different numerical specimens and their corresponding loading intensities. Each box represents the full range of displacement data, from the minimum value to the 16th percentile, median, 84th percentile, and maximum value. The displacements are limited to 60% of wall thickness as the collapse threshold. Specimens showing collapse in the simulations are highlighted with cross (×) marks

The probability-of-exceedance curves for peak OOP displacements, obtained from 29 simulations in each variation of the numerical models, are presented in Fig. 14. In each sub-figure, the curve corresponding to the specific variation is highlighted using a blue dash-dotted line. Alongside each curve, several statistical attributes of the displacement data are reported, including the minimum, maximum, mean, and standard deviation, and box plots representing the interval between the 16th and 84th percentiles. Additionally, each sub-figure includes a reference curve derived from the average displacements across all variations for each specimen, shown as a solid black line. The figure layout is structured such that the sub-figures in each column correspond to a particular damping assumption, while those in each row reflect variations based on specific loading conditions or material properties. For improved clarity, all displacement values are capped at 60% of wall thickness. Collapse events are marked with red circles.

Several key observations can be drawn from Fig. 14. First, displacement variations within the elastic regime are minimal. The median displacement across all variations ranges from 5% to 8% of wall thickness. However, beyond 20% of wall thickness, greater variability emerges, likely due to the high sensitivity of OOP displacements in the post-elastic response regime. Second, a reduction in damping leads to an increase in peak displacements, with lower damping values inducing higher displacements, as expected. The change in displacement demands is more pronounced when damping is reduced from 5% to 2.5%, compared to the reduction from 2.5% to 1.5%, further indicating that the original 5% damping assumption may have over-damped the specimens' dynamic response. It is also noteworthy that the expansion of the damping frequency range in V21–22 models has negligible impact on maximum displacements and collapses, reinforcing the robustness of the original damping calibration procedure based on the third and first natural frequencies. Third, simulations adopting raw input signals produce displacement comparable to those conducted with the cleaned input motions, suggesting that the essential characteristics of the loading signals are retained through the cleaning process. Fourth, while reducing the Young's modulus ($\mathrm{E_m}$) has only a minor effect on the response, increasing $\mathrm{E_m}$ leads to a significant reduction of deformations, particularly for displacements exceeding 25% of wall thickness. This is likely because the fundamental periods of the stiffer specimens shift towards lower-amplitude portions in the spectral content of the input motions, thereby reducing dynamic amplification effects. Finally, among the various parameters influencing joint nonlinear behavior, the softening length ($\mathrm{u_k}$) emerges as the most influential, followed by the friction coefficient ($\tan\phi$) and tensile strength ($\mathrm{f_t}$), in that order.

6 Blind-prediction contest response and comparison with experimental outcomes

The submissions made by the authors to each phase of the blind-prediction contest are discussed in this section and evaluated against the outcomes of the 29 experiments (Elmorsy et al. 2025) published after the conclusion of the contest. It is important to note that the experimental results are deliberately presented only in this final sub-section to maintain the emphasis of the paper on the blind-prediction process and the associated decision-making rationale adopted by the authors.

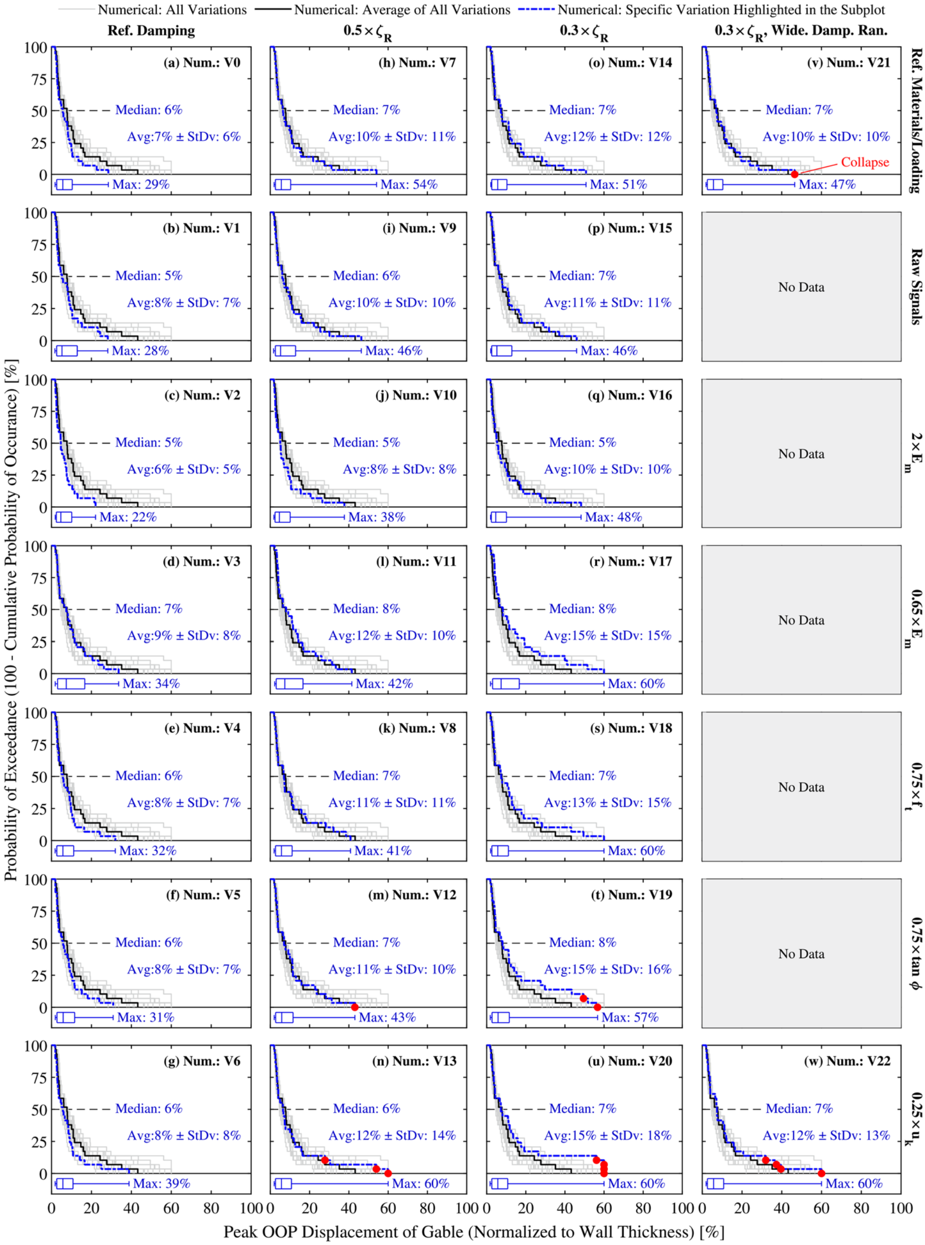

Fig. 14 The probability-of-exceedance curves of the peak OOP deformations observed in different variations of the numerical models. The data are shown in 23 sub-plots, with each one highlighting the curve of a single variation and comparing it against the average curve of all data. The variations are re-sorted for clear visualization of the influence of different modeling assumptions. The displacements are limited to 60% of wall thickness as the collapse threshold. Collapse is indicated with red circles

In accordance with the numerical results discussed in previous sections, the following response was submitted to the blind-prediction contest as the expected collapse probability and displacement demands:

- For collapse probability, a value of 0% was submitted in Phase 1, as none of the V0–V8 simulations, including V7 of Test 11 (House_11), which exhibited a peak OOP displacement as high as 54% of wall thickness, resulted in collapse. In Phase 2, additional simulation outcomes indicated that up to six specimens (House_11, House_12, House_13, House_14, House_27, and House_31) may have failed during the shake table tests (see Sect. 5.2), suggesting a potential collapse probability ranging from 0% to 17.2%. However, three of these specimens (House_12, House_13, and House_27) exhibited large-deformation responses in only a limited number of simulations, thereby reducing the confidence in predicting collapse for these cases. To resolve this uncertainty, an objective methodology was employed to determine which specimens should be declared as collapsed. For each of the six specimens, an individual collapse probability was calculated as the percentage of simulations in which a specimen exhibited deformation demands exceeding 25% of the wall thickness, taken as an indicator of potential collapse, over the total number of simulations conducted for that specimen (i.e., 23). Specimens with individual collapse probabilities exceeding 45%, namely House_11, House_12, House_14, and House_31, were identified as collapsed, resulting in a submitted overall collapse probability of 13.8% (4 out of 29 specimens) in the Phase 2 response. The threshold of 45% was selected instead of 50% to introduce conservativeness.
- Regarding displacement demands, the peak OOP displacement values submitted to the contest were not derived from a single model variation. Instead, the values were based on averages across multiple variations to account for uncertainties highlighted in the parametric study. Specifically, for Phase 1 predictions, the average of variations V0-8 was used, whereas for Phase 2, the average across all 23 variations was considered. This approach also mitigated the influence of artificially low and high displacements from high-damping (V0-6 with 5% damping) and low-damping (V14-22 with 1.5% damping) model variations, respectively. For specimens considered collapsed, displacement values were capped at 60% of wall thickness during the averaging process, under the assumption that specimens exhibiting deformations beyond this limit would have already experienced collapse (see Sect. 5.2).

Preliminary analysis of the experimental results (Elmorsy et al. 2025) reveals the following observations:

- In terms of collapse events, 4 out of the 29 specimens (House_28, House_29, House_30, and House_31) exhibit major collapse in the form of main wall OOP failure, as illustrated in Fig. 15. The main wall failure patterns resemble those obtained through numerical models (see Figure 11), as indicated in the figure. However, the tested specimens show a more dominant rocking in the opening flange and its OOP collapse before or during the failure of the main wall. In fact, 4 additional specimens (House_1, House_6, House_10, and House_24) demonstrate local failure in the form of rocking and OOP collapse of the opening flange.
- Regarding recorded deformation demands, the peak OOP displacements of the gable

obtained from the 29 experiments are presented in Fig. 16 individually for each specimen as black circles in Fig. 16a, and as a solid black probability-of-exceedance curve in Fig. 16b. The range of deformations predicted by the numerical models is represented by filled blue patches and agrees very well with the experimental outcomes. Again, the displacement values are limited to 60% of wall thickness for clear visualization. In Fig. 16a, specimens predicted to collapse in the numerical simulations are marked with blue crosses (×), while experimentally observed main wall collapses and flange collapses are denoted by black stars (*) and gray plus (+) signs, respectively. In Fig. 16b, probability-of-exceedance curves derived from averaging the outcomes of numerical simulations during Phase 1 (V0-8) and Phase 2 (V9-22) are shown via dashed red and dotted green lines, respectively, and the curve obtained from the average response of all numerical models is depicted via a dash-dotted blue line.

Comparison of the numerical predictions with the experimental outcomes highlights several important findings concerning the effectiveness of the proposed numerical modeling approach in satisfying the criteria of the contest:

- The numerical models successfully predict the occurrence of four main wall OOP collapses and reproduce collapse mechanisms consistent with those observed in the tests, thereby demonstrating the reliability of the proposed modeling approach and the accompanying sensitivity study. In particular, the inclusion of dynamic identification test data in Phase 2 significantly enhances the accuracy of the simulations by enabling the representation of main wall OOP collapse mechanisms.
- The numerical models do not reproduce the collapse of the opening flange perpendicular to the loading direction. This discrepancy may reflect deformation effects introduced by the centrifuge loading system that are not fully captured within the numerical framework adopted here. A possible misalignment between the intended and actual loading directions during testing could also have contributed to this outcome. Furthermore, the

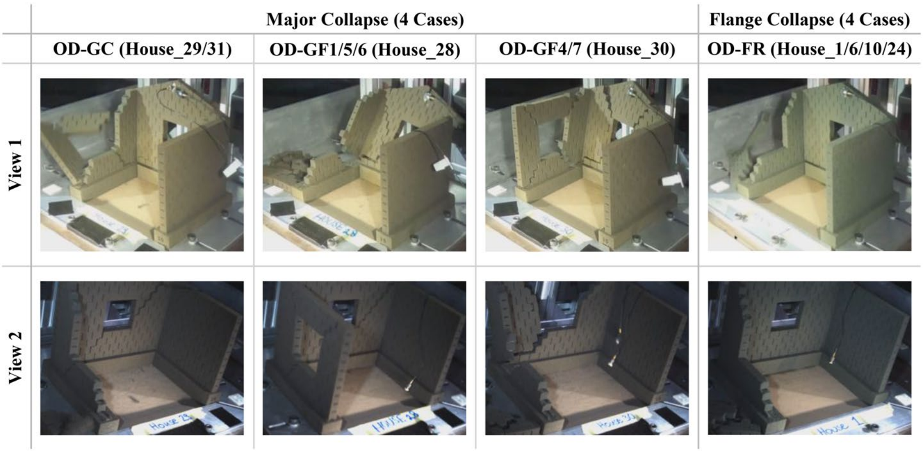

Fig. 15 Collapse mechanisms observed during benchmark experiments. These data are collected from the experimental dataset (Elmorsy et al. 2025) published after the conclusion of the blind-prediction contest. The experimental failure patterns are categorized based on the types of collapse observed in the numerical models, i.e., Fig. 11

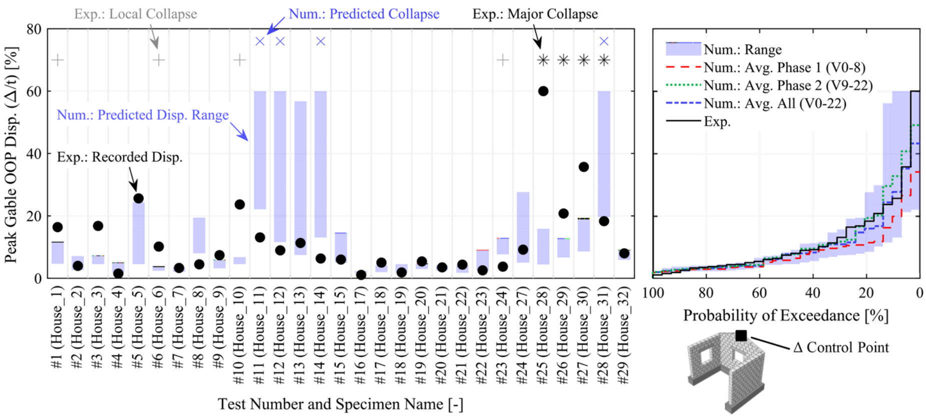

Fig. 16 Peak deformation demands observed during benchmark experiments: specimen-by-specimen (**a**) and as probability-of-exceedance curve (**b**). The experimental data are collected from the dataset (Elmorsy et al. 2025) published after the conclusion of the blind-prediction contest

prominent rocking of the opening flange observed experimentally may be linked to the minute differences in boundary conditions between the tests and the models. In the experiments, while the entire bottom surface of the main wall and solid flange is connected to the base, the opening flange is attached to the base only along its exterior quarter-thickness edges, creating a potential failure path that could be more easily activated under seismic motion. In the numerical models, this detail has been overlooked and not simulated, leading to a more symmetrical deformation of the modeled sub-structures. Finally, the mismatch between first-mode frequencies of the numerical and experimental specimens may have also been a reason.

- Although the total number of main wall OOP collapses is accurately predicted, three out of four specimens identified as vulnerable to collapse in the simulations (House_11, House_12, House_14) differ from those that have collapsed in the experiments (House_28, House_29, House_30) and only House_31 is correctly predicted to collapse. This discrepancy may arise from the small-scale nature of the experimental specimens, which can introduce additional uncertainties regarding physical scaling effects, such as those related to air viscosity, that are not reflected in the up-scale numerical models. Differences may also stem from variations in the modal properties of the numerical and experimental specimens causing them to behave differently under each ground-motion. Uncertainties inherent in the dynamic response of masonry, as well as to factors such as the environmental and loading conditions during the experiments, which are difficult to replicate in a numerical framework without access to supporting experimental data, may have also played a role.
- The numerical models exhibit strong performance in predicting peak deformation demands. Experimental measurements of peak gable OOP displacements fall within or marginally outside the numerically predicted range for 20 out of 29 (approximately 70% of the) specimens, showing reasonable performance in the deterministic prediction of the responses.
- More pronounced discrepancies between the predicted and actual deformation demands are observed in nine specimens (House_1, House_3, House_6, House_10, House_11,

House_14, House_28, House_29, and House_30), six of which correspond to experimental collapses (main wall or flange) not predicted numerically (House_1, House_6, House_10, House_28, House_29, and House_30), and one to a numerical collapse not observed in the experiments (House_14), highlighting again the complexity of accurately predicting the dynamic OOP response in the post-peak regime.
- When considering probability-of-exceedance curves rather than individual specimen responses, experimentally derived curves align closely with the numerical simulation range. This suggests that discrepancies in predicted deformation demands are driven primarily by differences in collapse occurrence rather than by inaccuracies in the numerical modeling approach. Moreover, the results underscore the chaotic nature of dynamic OOP behaviors, which cannot be predicted deterministically but should instead be addressed within a multi-variational framework, such as the one used in this study and enabled by the developed modeling approach.
- The experimentally derived probability-of-exceedance curve lies between the average curves obtained from Phase 1 and Phase 2 simulations, with a lower margin of deviation from the Phase 2 average curve. This indicates that access to modal identification data in Phase 2 enhances predictions of displacement demands. Moreover, the average probability-of-exceedance curve from the combined outcomes of Phase 1 and 2 lies even closer to the experimental one, suggesting that different variations of low and high damping should be considered to allow accurate representation of variability in the test outcomes.

Based on the above comparison, the numerical modeling approach is considered representative of the global experimental behavior in terms of collapse onset, failure mechanisms, and deformation demands. Moreover, as judged by the organizers of the PEER campaign, the predictions of this study provide the closest approximation to the experimental response in both phases of the blind-prediction contest among all participants using different modeling approaches. In evaluating the submissions to each phase of the contest, the organizers calculate the prediction error for the probability of collapse as the absolute difference between the number of predicted and actual collapses, normalized by the total number of tests. They also calculate the predictive error for the deformation demands as the maximum absolute difference between the predicted and actual probability of exceedance at any peak OOP displacement. The combined error derived from these two calculations is used to grade the submissions. Based on this grading system, the submission of this study yields total errors of 0.586 and 0.448 in Phases 1 and 2 of the contest, respectively, where the ranges of total errors across all contestants are 0.586–1.241 in Phase 1 and 0.448–1.034 in Phase 2.

Despite the excellent outcome of the contest and the good prediction of deformation demands, the predictive performance for the probability of collapse should be discussed. Specifically, given the challenges faced in this study regarding the capture of real collapse in the numerical simulations, the importance of using the 25% deformation threshold should be highlighted, and the robustness of this choice should be discussed. Although a comprehensive investigation of the most fitting deformation threshold was beyond the scope of this study, a simple exercise was performed to investigate the performance of higher and lower thresholds. Specifically, 20 and 30% of wall thickness were used to re-identify the number of collapsed specimens in the numerical simulations of this study. Lower and higher thresholds were not investigated, as they were deemed too conservative and non-conservative, respectively, and did not correspond to the range of thresholds observed in the current and previous studies, as explained in Sect. 5.2. In the new calculations, the use of both 20 and 30% thresholds led to identifying four collapses, similar to when the 25% threshold was used. This shows that the outcomes of the current study would not have changed with the use of a different collapse-detection threshold, and that a deformation threshold within the range of 20–30% of wall thickness can be effectively used in future studies to indicate the collapse of two-way spanning walls.

Finally, it should be noted that the numerical up-scaling procedure employed in this study may not fully capture certain physical effects of scaling. Although, this limitation is not further examined, since all validation checks conducted to ensure similitude between the 1:15-scale and full-scale numerical models, including stresses, strains, reaction forces, frequencies, masses, stiffnesses, and nonlinear behaviors, confirm full compliance with the similitude law adopted in the experiments.

7 Conclusions

This paper presents a numerical modeling approach developed for the blind prediction of the out-of-plane (OOP) dynamic response of 3D-printed masonry-like structures subjected to seismic ground motions via shake table loading. The 3D block-based model, originally developed by the authors for high-fidelity simulation of the dynamic behavior of one- and two-way spanning unreinforced masonry walls, is extended here to simulate the response of 1:15-scale 3D-printed masonry-like sub-structures tested at the Geotechnical Centrifuge Center of Eidgenössische Technische Hochschule Zürich (ETH Zürich, Switzerland) as part of the experimental campaign organized by the Pacific Earthquake Engineering Research Center (PEER, USA), the National Technical University of Athens (NTU Athens, Greece), and ETH Zürich. The specimens are modeled by idealizing their "homogeneous" typology within a "discrete" block-and-joint framework and scaling them up to the full 1:1 scale. Multiple variations of the numerical models are developed to account for uncertainties in loading signal characteristics, material properties in both the elastic and nonlinear regimes, and damping ratios representative of experimental conditions. The rationale and outputs of 667 nonlinear time-history analyses across 23 model variations and 29 ground motion records are presented, and the results are evaluated in terms of collapse probability, failure mechanisms, and peak OOP displacement demands. The predictions submitted for the blind-prediction contest are then compared with experimental outcomes, published only after the contest, to assess the effectiveness of the numerical approach, particularly the adaptations introduced to represent the PEER sub-structure typology. The main findings are as follows:

- The back-scaling methodology, which consists of magnifying the geometry to 1:1 scale, converting material parameters to full-scale equivalents, and reverse-processing the loading signals to their real-world intensities and spectral content, proves effective in maintaining similitude between the static, modal, and dynamic responses of the full-scale and original small-scale specimens. However, potential limitations remain, particularly regarding unaccounted physical effects of scaling, such as the influence of air viscosity on dynamic responses.
- The sensitivity study and blind-prediction rationale, including the use of 25% of wall

thickness as a collapse threshold, closely match the experimental outcomes in terms of peak OOP displacements and number of major failures, resulting in the most accurate predictions among all participants. Thresholds corresponding to 20 and 30% of the wall thickness showed similar predictive performance, suggesting that a 20–30% range can be used for numerical collapse detection in two-way spanning walls.

- Major failure in the form of OOP collapse of the main wall is simulated with high consistency relative to experimental observations, and the number of specimens exhibiting this failure mode is predicted in agreement with test results. In contrast, local failure involving in-plane rocking followed by OOP collapse of the flanges is not captured numerically, likely due to experimental uncertainties such as loading direction and potential effects introduced by the centrifuge apparatus, as well as the mismatches between modal behavior of the numerical and experimental specimens.
- Peak OOP displacement demands are accurately reproduced for approximately 70% of specimens, with discrepancies limited to nine specimens showing actual or potential collapse. The probability-of-exceedance curve, based on peak OOP displacements averaged across all numerical variations, shows close agreement with the experimental curve.
- Large scatter is observed across displacement demands obtained from different numerical variations for specimens approaching collapse, highlighting the increased uncertainty and chaotic dynamic behavior of masonry once nonlinear responses begin. Regarding parameter influence, damping ratio, brittleness, friction coefficient, and tensile strength had the greatest impact on predictions, with only the first two exerting a major effect.
- Access to information regarding the modal response of the experimental specimens, provided only during Phase 2 of the contest, significantly improves the ability of the numerical simulations to capture collapse and enables more reliable predictions of displacement demand ranges.
- Because the number of major collapses or severely damaged cases observed in the experiments and numerical models is limited, and because the applied records vary in intensity, record-to-record variability in failure mechanisms cannot be assessed comprehensively. Nonetheless, the influence of ground motion characteristics on damage patterns, displacement demands, and collapse probability is clearly evident from both the experimental and numerical outcomes.

This study provided two key contributions. First, it developed a modeling strategy capable of representing the complex geometries of 3D-printed masonry-like specimens and in capturing their structural-scale static and dynamic behaviors, particularly from a probabilistic perspective. This modeling strategy provides a useful basis for future numerical studies of 3D-printed concrete structures, for which standardized approaches are still emerging. Second, it formulated a parametric blind-prediction workflow that can be used in the future studies to accommodate the sensitive nature of masonry dynamic responses, particularly in near-collapse conditions. While the study also advances the understanding of record-to-record variability and numerical modeling under uncertainty, further development is needed to enable more systematic sensitivity analyses. Future work should explore the use of loading signals with comparable intensity levels but different spectral content to isolate the influence of specific motion characteristics.

8 Appendix: Visualization of raw loading signals and the processed ones

The motions recorded at the shake table in the loading direction during each of the 29 benchmark tests are shown in Fig. 17 in terms of acceleration and displacement time histories, as well as spectral acceleration and displacement data. It should be noted that only the acceleration time histories were provided in the blind-prediction contest data (Elmorsy et al. 2025) and the rest of the curves are derived during this study. Figure 18 presents the cropped and cleaned versions of these loading signals, processed in this study, along with their corresponding displacement and spectral content. For consistency and ease of comparison, each signal is shown using same via color across the two figures. Additionally, Fig. 19 illustrates the variations in key signal properties resulting from the cropping and cleaning procedure of this study. Several observations can be made. First, cropping proves effective, reducing the loading durations by 10–95%, thereby enabling more efficient analyses (Fig. 19a). Second, the cleaning process does not introduce significant changes in loading intensity (Fig. 19b), with only a few signals showing variations, limited to a maximum of 7.7%. Third, although changes in acceleration time histories are minor (Figs. 17a and 18a), the spectral acceleration of five signals (used in Tests 8, 14, 15, 21, and 24) exhibits noticeable changes after cleaning (Figs. 17c and 18c), with peak spectral acceleration increasing by up to 71% and the corresponding period reducing by up to 62% (Fig. 19b). Fourth, despite these spectral changes, the resultant displacement time histories (Fig. 17b and 18b) and displacement spectra (Fig. 17d and 18d) of the processed signals remain closely aligned with those of the

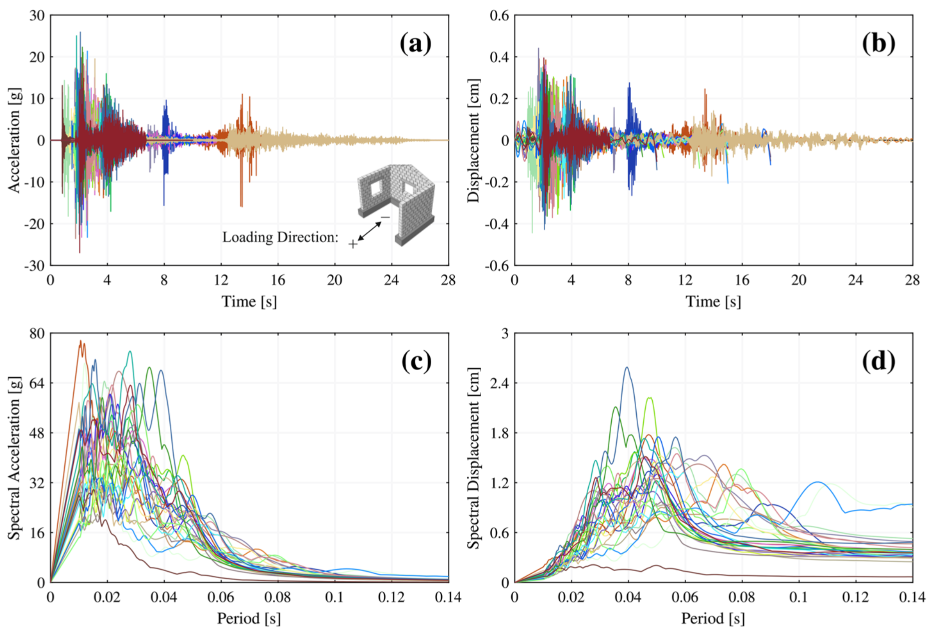

Fig. 17 Raw dynamic loading signals "recorded" in the shake-table tests of the PEER experimental campaign (Elmorsy et al. 2025): acceleration (**a**) and displacement (**b**) time histories and spectral acceleration (**c**) and displacement (**d**) content of the 1:15-scaled signals. The curves of each signal are highlighted with a different color. These signals are collected from the accelerometer attached to the shaking table

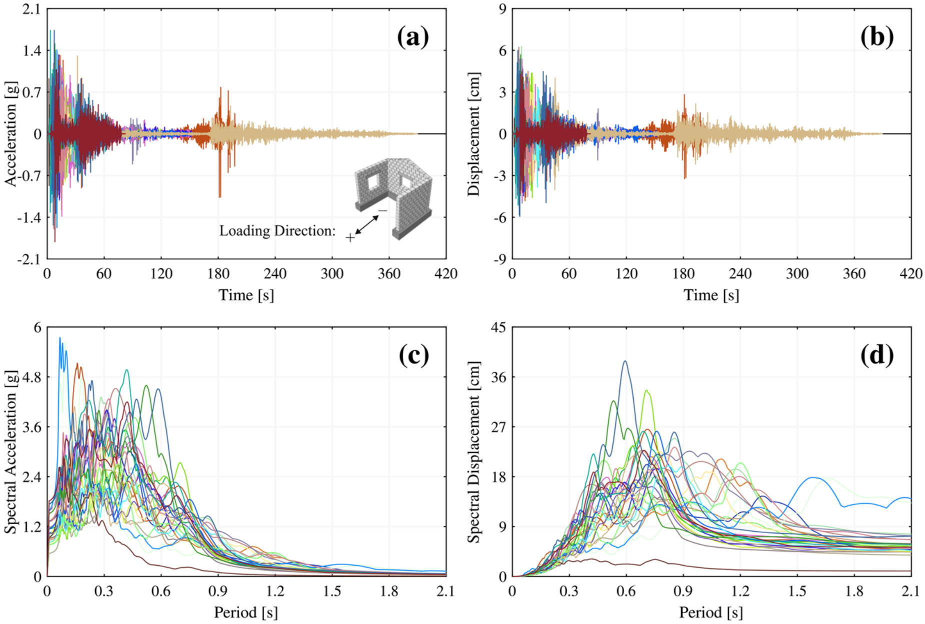

Fig. 18 Processed dynamic loading signals "used" in the current numerical simulations of PEER shake table tests: acceleration (**a**) and displacement (**b**) time histories and spectral acceleration (**c**) and displacement (**d**) content of the 1:1-scaled cropped and cleaned signals. The curves of each signal are highlighted with a different color. These signals are resulted from the processing applied in the current study

raw signals, with negligible differences in spectral displacement (Fig. 19c). While the displacement properties are well preserved, the altered spectral accelerations in the five signals may have influenced simulation outcomes. Specifically, in the simulations of tests 8, 14, and 21 (House_8, House_14, and House_22), the experimentally recorded displacement falls below the range predicted by the numerical simulations (Fig. 16). However, as this effect is only significant in one case (House_14), and no meaningful difference is observed between simulations using raw or processed signals (see Sect. 5), these discrepancies are not considered to have impacted the overall statistical approach adopted in this study.

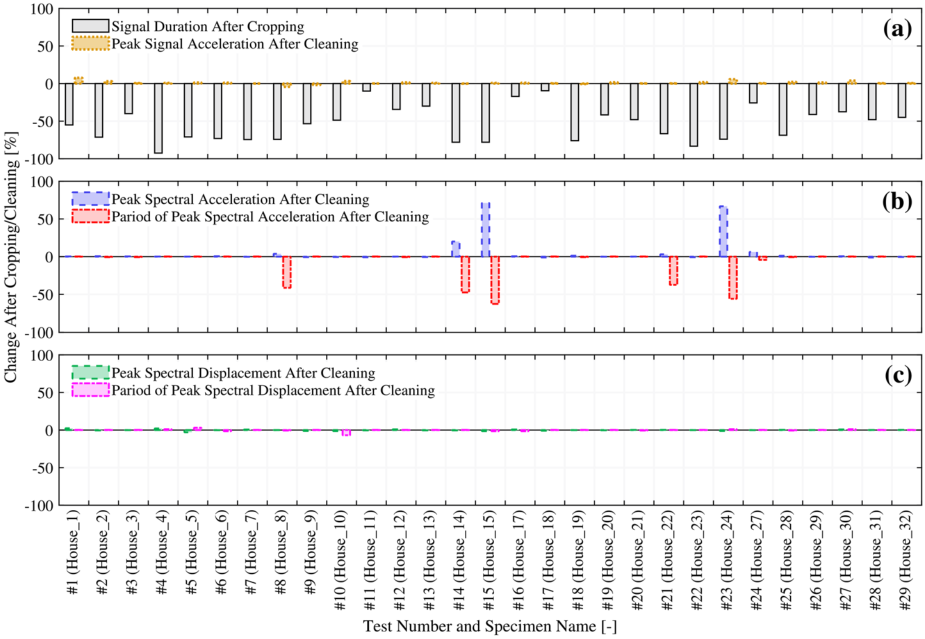

Fig. 19 Variations in the loading accelerograms after cropping and cleaning applied in the current study: reduction in duration after cropping and change peak acceleration after cleaning (**a**), changes in peak spectral acceleration and the period corresponding to it after cleaning (**b**), changes in peak spectral displacement and the period corresponding to it after cleaning (**c**)

Acknowledgements All experimental data used as a benchmark in this paper was collected from the PEER 2025 Blind-Prediction Contest titled "Shaking Table Tests on 29 Masonry Model Structures" (Pacific Earthquake Engineering Research Center PEER 2025; Del Giudice et al. 2024).

Author contributions AG: Conceptualization, Methodology, Software, Validation, Formal analysis, Investigation, Resources, Data Curation, Writing – Original Draft, Writing – Review and Editing, Visualization. AA: Methodology, Validation, Writing – Review and Editing, Supervision. AMD: Methodology, Validation, Writing – Review and Editing, Supervision, Funding Acquisition. SS: Methodology, Validation, Writing – Review and Editing, Supervision. FM: Methodology, Validation, Writing – Review and Editing, Supervision, Funding Acquisition.

Funding This research was conducted as part of the scientific consolidation of projects funded by Nederlandse Aardolie Maatschappij (NAM) BV under contract number UI46268 "Physical testing and modeling–Masonry structures Groningen", which is gratefully acknowledged. This work was partially supported by ReLUIS and the Italian Department of Civil Protection, as part of the activity was carried out in the framework of the ReLUIS-DPC Project 2024–2026–Work Package 10 (Masonry structures), Task 10.1.

Data availability The datasets generated during the current study are available from the corresponding author upon reasonable request.

Declarations

Competing interests The authors have no relevant financial or non-financial interests to disclose.

References

Ancheta TD, Darragh RB, Stewart JP, Seyhan E, Silva WJ, Chiou BS-J, Wooddell KE, Graves RW, Kottke AR, Boore DM, Kishida T, Donahue JL (2014) NGA-West2 database. Earthq Spectra 30(3):989–1005. https://doi.org/10.1193/070913EQS197M

Anić F, Penava D, Abrahamczyk L, Sarhosis V (2020) A review of experimental and analytical studies on the out-of-plane behaviour of masonry infilled frames. Bull Earthq Eng 18(5):2191–2246. https://doi.org/10.1007/s10518-019-00771-5

Aşıkoğlu A, Avşar Ö, Lourenço PB, Silva LC (2019) Effectiveness of seismic retrofitting of a historical masonry structure: Kütahya Kurşunlu Mosque, Turkey. Bull Earthq Eng 17(6):3365–3395. https://doi.org/10.1007/s10518-019-00603-6

Baek ER, Pohoryles DA, Bournas D (2024) Seismic assessment of the in-plane/out-of-plane interaction of masonry infills in a two-storey RC building subjected to bi-directional shaking table tests. Earthq Eng Struct Dyn 53(6):2230–2251. https://doi.org/10.1002/eqe.4109

Bayrak AT, Shaban N, Seyedian Choubi S, Tuncer E, Yang S-H, Yılmaz HD, Alkilani AZ, Dal H, Unluer C, Dino G, Örtemiz E, Sarıtaş A, Meral Akgul C (2024) Spatial variation of physical, mechanical, and thermophysical properties of 3D printed concrete across a full-scale wall. Constr Build Mater 431:136574. https://doi.org/10.1016/j.conbuildmat.2024.136574

Boore DM, Bommer JJ (2005) Processing of strong-motion accelerograms: needs, options and consequences. Soil Dyn Earthq Eng 25(2):93–115. https://doi.org/10.1016/j.soildyn.2004.10.007

Bui TT, Limam A (2014) Out-of-plane behaviour of hollow concrete block masonry walls unstrengthened and strengthened with CFRP composite. Compos B Eng 67:527–542. https://doi.org/10.1016/j.compositesb.2014.08.006

Caicedo D, Hussaini SMS, Karimzadeh S, Bernardo V, Lourenço PB (2024a) Seismic assessment of masonry structures by means of code-based selected records. J Phys Conf Ser 2647(14):142001. https://doi.org/10.1088/1742-6596/2647/14/142001

Caicedo D, Tomić I, Karimzadeh S, Bernardo V, Beyer K, Lourenço PB (2024b) Collapse fragility analysis of historical masonry buildings considering in-plane and out-of-plane response of masonry walls. Eng Struct 319:118804. https://doi.org/10.1016/j.engstruct.2024.118804

Caicedo D, Karimzadeh S, Bernardo V, Lourenço PB (2024) Selection and scaling approaches of earthquake time-series for structural engineering applications: a state-of-the-art review. Arch Computat Methods Eng 31(3):1475–1505. https://doi.org/10.1007/s11831-023-10025-y

Caicedo D, Tomić I, Karimzadeh S, Bernardo V, Beyer K, Lourenço PB (2025) Code-based ground motion selection and scaling for seismic assessment: application to two masonry building case studies. J Build Eng 111:113558. https://doi.org/10.1016/j.jobe.2025.113558

Candeias PX, Costa AC, Mendes N, Costa AA, Lourenço PB (2016a) Experimental assessment of the out-of-plane performance of masonry buildings through shaking table tests. Int J Architectural Heritage 1–28. https://doi.org/10.1080/15583058.2016.1238975

Candeias PX, Costa AC, Mendes N, Costa AA, Lourenço PB (2016b) Experimental assessment of the out-of-plane performance of masonry buildings through shaking table tests. Int J Architectural Heritage 11:1–28. https://doi.org/10.1080/15583058.2016.1238975

Canditone C, Parisi F, D'Ayala DF, Guardiola-Villora A (2025) Seismic collapse analysis of unreinforced masonry buildings through applied element micro-modelling and crack width-based damage measures. Bull Earthq Eng 23(11):4719–4753. https://doi.org/10.1007/s10518-025-02231-9

Chong VL (1993) The behaviour of laterally loaded masonry panels with openings. Ph.D. Dissertation

Cima V, Tomei V, Grande E, Imbimbo M (2023) Fragility curves for residential unreinforced masonry buildings prone to out-of-plane mechanisms: the case of the historical center of Sora. Procedia Struct Integr 44:211–218. https://doi.org/10.1016/j.prostr.2023.01.028

Cima V, Tomei V, Grande E, Imbimbo M (2024) Fragility curves for the seismic assessment of masonry buildings in historic centres prone to out-of-plane failure modes. Bull Earthq Eng 22(4):1801–1826. https://doi.org/10.1007/s10518-023-01831-7

D'Altri AM, de Miranda S, Castellazzi G, Sarhosis V (2018) A 3D detailed micro-model for the in-plane and out-of-plane numerical analysis of masonry panels. Comput Struct 206:18–30. https://doi.org/10.1016/j.compstruc.2018.06.007

D'Altri AM, Messali F, Rots J, Castellazzi G, de Miranda S (2019) A damaging block-based model for the analysis of the cyclic behaviour of full-scale masonry structures. Eng Fract Mech 209:423–448. https://doi.org/10.1016/j.engfracmech.2018.11.046

D'Ayala DF, Paganoni S (2011) Assessment and analysis of damage in L'Aquila historic city centre after 6th April 2009. Bull Earthq Eng 9(1):81–104. https://doi.org/10.1007/s10518-010-9224-4

Damiola M, Esposito R, Messali F, Rots JG (2018) Quasi-static cyclic two-way out-of-plane bending tests and analytical models comparison for URM walls. In: 10th International Masonry Conference, Milan, Italy

Dauda JA, Iuorio O, Muhit IB, da Silva LCM (2024) Systematic review of experimental testing of masonry walls' failure: comparative analysis and future directions. Eng Fail Anal 163:108571. https://doi.org/10.1016/j.engfailanal.2024.108571

De Felice G, Giannini R (2001) Out-of-plane seismic resistance of masonry walls. J Eart Eng 5(2):253–271. https://doi.org/10.1080/13632460109350394

Del Giudice L, Katsamakas A, Liu B, Sarhosis V, Vassiliou MF (2024) Physical modelling of unreinforced masonry walls using a sand-based 3D printer. Eng Struct 305:117665. https://doi.org/10.1016/j.engstruct.2024.117665

Derakhshan H, Lucas W, Visintin P, Griffith MC (2018) Out-of-plane strength of existing two-way spanning solid and cavity unreinforced masonry walls. Structures 13:88–101. https://doi.org/10.1016/j.istruc.2017.11.002

Elmorsy M, Jones L, Wild M, Katsamakas A, Tatsis K, Anastasopoulos I, Vassiliou M (2026) Benchmark dataset from centrifuge shake table tests of 3D-printed unreinforced masonry structures for seismic model validation. Earthq Spectra 42(1). https://doi.org/10.1002/esp4.70042

Elmorsy M, Jones LA, Wild M et al (2025) Dataset from shake table centrifuge tests of 3D printed unreinforced masonry structures. Zürich, Switzerland

Ewins DJ (2000) Modal testing: theory, practice, and application. Research Studies Press

Frankie TM, Gencturk B, Elnashai AS (2013) Simulation-based fragility relationships for unreinforced masonry buildings. J Stru Eng 139(3):400–410. https://doi.org/10.1061/(ASCE)ST.1943-541X.0000648

Gentile C, Saisi A (2007) Ambient vibration testing of historic masonry towers for structural identification and damage assessment. Constr Build Mater 21(6):1311–1321. https://doi.org/10.1016/j.conbuildmat.2006.01.007

Gesualdi G, Viggiani LRS, Cardone D (2020) Seismic performance of RC frame buildings accounting for the out-of-plane behavior of masonry infills. Bull Earthq Eng 18(11):5343–5381. https://doi.org/10.1007/s10518-020-00904-1

Ghezelbash A, Messali F, Rots JG (2023) Challenges in the calibration of finite element models for the analysis of masonry structures: a comparative study. In: XVII International Conference on Computational Plasticity, Fundamentals and Applications, Barcelona, Spain

Ghezelbash A, D'Altri AM, Sharma S, Lourenço PB, Rots JG, Messali F (2025a) A block-based numerical strategy for modeling the dynamic out-of-plane behavior of unreinforced brick masonry walls. Meccanica 60(7):2069–2105. https://doi.org/10.1007/s11012-024-01899-8

Ghezelbash A, Sharma S, D'Altri AM, Lourenço PB, Rots JG, Messali F (2025b) Challenges in high-fidelity implicit block-based numerical simulation of dynamic out-of-plane two-way bending in unreinforced brick masonry walls. Earthq Eng Struct Dyn 54(7):1836–1858. https://doi.org/10.1002/eqe.4337

Ghezelbash A, D'Altri AM, Lourenço PB, de Miranda S (2026a) Numerical modeling of the out-of-plane dynamic response of masonry gable walls via a high-fidelity block-based finite element modeling approach – part I: blind prediction. Bull Earthq Eng. https://doi.org/10.1007/s10518-025-02328-1

Ghezelbash A, D'Altri AM, Sharma S, Lourenço PB, de Miranda S, Messali F (2026b) Numerical modeling of the out-of-plane dynamic response of masonry gable walls via a high-fidelity block-based finite element modeling approach – part II: post-diction and application to other structural configurations. Bull Earthq Eng. https://doi.org/10.1007/s10518-026-02473-1

Ghezelbash A, Sharma S, Rots JG, Messali F (2026c) Effects of relative support motions on the out-of-plane dynamics of one-way spanning unreinforced masonry walls and insights into instability displacement. J Struct Eng 152(7). https://doi.org/10.1061/JSENDH.STENG-15104

Giaretton M, Dizhur D, Ingham JM (2016) Dynamic testing of as-built clay brick unreinforced masonry parapets. Eng Struct 127:676–685. https://doi.org/10.1016/j.engstruct.2016.09.016

Giordano N, De Luca F, Sextos A (2021) Analytical fragility curves for masonry school building portfolios in Nepal. Bull Earthq Eng 19(2):1121–1150. https://doi.org/10.1007/s10518-020-00989-8

Giordano N, De Risi R, Voyagaki E, Kloukinas P, Novelli V, Kafodya I, Ngoma I, Goda K, Macdonald J (2021) Seismic fragility models for typical non-engineered URM residential buildings in Malawi. Structures 32:2266–2278. https://doi.org/10.1016/j.istruc.2021.03.118

Girardi M, Padovani C, Pellegrini D, Robol L (2021) A finite element model updating method based on global optimization. Mech Syst Signal Process 152:107372. https://doi.org/10.1016/j.ymssp.2020.107372

Graziotti F, Tomassetti U, Penna A, Magenes G (2016) Out-of-plane shaking table tests on URM single leaf and cavity walls. Eng Struct 125:455–470. https://doi.org/10.1016/j.engstruct.2016.07.011

Graziotti F, Tomassetti U, Sharma S, Grottoli L, Magenes G (2019) Experimental response of URM single leaf and cavity walls in out-of-plane two-way bending generated by seismic excitation. Constr Build Mater 195:650–670. https://doi.org/10.1016/j.conbuildmat.2018.10.076

Griffith MC, Lam NTK, Wilson JL, Doherty K (2004) Experimental investigation of unreinforced brick masonry walls in Flexure. J Stru Eng 130(3):423–432. https://doi.org/10.1061/(ASCE)0733-9445(2004)130:3(423)

Griffith MC, Vaculik J, Lam NTK, Wilson J, Lumantarna E (2007) Cyclic testing of unreinforced masonry walls in two-way bending. Earthq Eng Struct Dyn 36(6):801–821. https://doi.org/10.1002/eqe.654

Harris H, Sabnis GM (1999) Structural modeling and experimental techniques. CRC Press

Hendry EAW (2001) Masonry walls: materials and construction. Constr Build Mater 15(8):323–330. https://doi.org/10.1016/S0950-0618(01)00019-8

Hibbitt D, Karlsson B, Sorensen P (2011) Abaqus/CAE user's manual. Dassault Systèmes SE, United States

Hilber HM, Hughes TJR, Taylor RL (1977) Improved numerical dissipation for time integration algorithms in structural dynamics. Earthq Eng Struct Dyn 5(3):283–292. https://doi.org/10.1002/eqe.4290050306

Jafari S (2021) Material characterisation of existing masonry: a strategy to determine strength, stiffness and toughness properties for structural analysis. Ph.D. Dissertation

Kadysiewski S, Mosalam KM (2009) Modeling of unreinforced masonry infill walls considering in-plane and out-of-plane interaction. University of California, Berkeley, United States

Kallioras S, Graziotti F, Penna A, Magenes G (2022) Effects of vertical ground motions on the dynamic response of URM structures: comparative shake-table tests. Earthq Eng Struct Dyn 51(2):347–368. https://doi.org/10.1002/eqe.3569

Kaya A, Adanur S, Bello RA, Genç AF, Okur FY, Sunca F, Günaydin M, Altunişik AC, Sevim B (2023) Post-earthquake damage assessments of unreinforced masonry (URM) buildings by shake table test and numerical visualization. Eng Fail Anal 143:106858. https://doi.org/10.1016/j.engfailanal.2022.106858

Kesavan P, Menon A (2022) Investigation of in-plane and out-of-plane interaction in unreinforced masonry piers by block-based micro-modeling. Structures 46:1327–1344. https://doi.org/10.1016/j.istruc.2022.10.105

Kesavan P, Menon A (2023) A macro-element with bidirectional interaction for seismic analysis of unreinforced masonry walls. Earthq Eng Struct Dyn 52(6):1740–1761. https://doi.org/10.1002/eqe.3841

Liang C (1996) Experimental and theoretical investigation of the behaviour of brickwork cladding panel subjected to lateral loading. Ph.D. Dissertation

Losanno D, Ravichandran N, Parisi F (2023) Seismic fragility models for base-isolated unreinforced masonry buildings with fibre-reinforced elastomeric isolators. Earthq Eng Struct Dyn 52(2):308–334. https://doi.org/10.1002/eqe.3761

Lourenço PB (2000) Anisotropic softening model for masonry plates and shells. J stru Eng 126(9):1008–1016. https://doi.org/10.1061/(ASCE)0733-9445(2000)126:9(1008)

Lourenço PB (2004) Current experimental and numerical issues in masonry research. In: Proceedings of the 13th International Brick and Block Masonry Conference, Amsterdam, Netherlands

Macorini L, Izzuddin BA (2011) A non-linear interface element for 3D mesoscale analysis of brick-masonry structures. Int J Numer Methods Eng 85(12):1584–1608. https://doi.org/10.1002/nme.3046

Malomo D, DeJong MJ (2022) A macro-distinct element model (M-DEM) for simulating in-plane/out-of-plane interaction and combined failure mechanisms of unreinforced masonry structures. Earthq Eng Struct Dyn 51(4):793–811. https://doi.org/10.1002/eqe.3591

Malomo D, Pinho R, Penna A (2020) Numerical modelling of the out-of-plane response of full-scale brick masonry prototypes subjected to incremental dynamic shake-table tests. Eng Struct 209:110298. https://doi.org/10.1016/j.engstruct.2020.110298

Mohyeddin A, Goldsworthy HM, Gad EF (2013) FE modelling of RC frames with masonry infill panels under in-plane and out-of-plane loading. Eng Struct 51:73–87. https://doi.org/10.1016/j.engstruct.2013.01.012

Moon L, Dizhur D, Senaldi I, Derakhshan H, Griffith M, Magenes G, Ingham J (2014) The demise of the URM building stock in christchurch during the 2010–2011 canterbury earthquake sequence. Earthq Spectra 30(1):253–276. https://doi.org/10.1193/022113EQS044M

Moshfeghi A, Smyrou E, Arslan O, Engin Bal I (2024) Out-of-plane shake table tests on solid masonry walls with timber floors. Structures 66:106815. https://doi.org/10.1016/j.istruc.2024.106815

Mucedero G, Perrone D, Monteiro R (2022) Epistemic uncertainty in poorly detailed existing frames accounting for masonry infill variability and RC shear failure. Earthq Eng Struct Dyn 51(15):3755–3778. https://doi.org/10.1002/eqe.3748

Nale M, Benvenuti E, Chiozzi A, Minghini F, Tralli A (2023) Effect of uncertainties on seismic fragility for out-of-plane collapse of unreinforced masonry walls. J Build Eng 75:106936. https://doi.org/10.1016/j.jobe.2023.106936

Nie Y, Sheikh A, Visintin P, Griffith M (2023) A robust computational strategy for failure prediction of masonry structures using an improved multi-surface damage-plastic based interface model. Int J Numer Methods Eng 124(11):2498–2528. https://doi.org/10.1002/nme.7218

Noor-E-Khuda S (2021) An explicit finite-element modeling method for masonry walls using continuum shell element. J Archit Eng 27(4):1–15. https://doi.org/10.1061/(ASCE)AE.1943-5568.0000518

Noor-E-Khuda S, Dhanasekar M, Thambiratnam DP (2016) An explicit finite element modelling method for masonry walls under out-of-plane loading. Eng Struct 113:103–120. https://doi.org/10.1016/j.engstruct.2016.01.026

Oktiovan YP, Messali F, Pulatsu B, Lemos JV, Rots JG (2024) A contact-based constitutive model for the numerical analysis of masonry structures using the distinct element method. Comput Struct 303:107499. https://doi.org/10.1016/j.compstruc.2024.107499

Oyarzo-Vera C, Griffith MC (2009) The Mw 6.3 Abruzzo (italy) earthquake of april 6th, 2009: on site observations. Bull N Z Soc Earthq Eng 42(4):302–307. https://doi.org/10.5459/bnzsee.42.4.302-307

Pacific Earthquake Engineering Research Center PEER 2025 Blind prediction contest: shaking table tests on 29 masonry model structures. 2025. In: https://peer.berkeley.edu/news-and-events/2025-blind-prediction-contest

Padalu PKVR, Singh Y, Das S (2020) Cyclic two-way out-of-plane testing of unreinforced masonry walls retrofitted using composite materials. Constr Build Mater 238:117784. https://doi.org/10.1016/j.conbuildmat.2019.117784

Page AW (1991) The Newcastle Earthquake - behaviour of masonry structures. Masonry Int 5:11–18

Penna A, Morandi P, Rota M, Manzini CF, da Porto F, Magenes G (2014) Performance of masonry buildings during the Emilia 2012 earthquake. Bull Earthq Eng 12(5):2255–2273. https://doi.org/10.1007/s10518-013-9496-6

Penner O, Elwood KJ (2016) Out-of-plane dynamic stability of unreinforced masonry walls in one-way bending: shake table testing. Earthq Spectra 32(3):1675–1697. https://doi.org/10.1193/011415EQS009M

Rots JG, Messali F, Esposito R et al (2016) Thematic Keynote Computational modelling of masonry with a view to Groningen induced seismicity. In: 10th International Conference on Structural Analysis of Historical Constructions, Leuven, Belgium

Selby RG, Vecchio FJ (1993) Three-dimensional constitutive relations for reinforced concrete. University of Toronto

Sharma S, Silva LC, Graziotti F, Magenes G, Milani G (2021) Modelling the experimental seismic out-of-plane two-way bending response of unreinforced periodic masonry panels using a non-linear discrete homogenized strategy. Eng Struct 242:112524. https://doi.org/10.1016/j.engstruct.2021.112524

Sharma S, Tomassetti U, Grottoli L, Graziotti F (2020) Two-way bending experimental response of URM walls subjected to combined horizontal and vertical seismic excitation. Eng Struct 219:110537. https://doi.org/10.1016/j.engstruct.2020.110537

Simsir CC, Aschheim MA, Abrams D (2004) Out-of-plane dynamic response of unreinforced bearing walls attached to flexible diaphragms. In: Proceedings of 13th World Conference on Earthquake Engineering, Vancouver, BC, Canada

Simsir CC, Aschheim MA, Abrams DP (2004) Out-of-plane dynamic response of unreinforced bearing walls attached to flexible diaphragms. In: Proceedings of 13th World Conference on Earthquake Engineering, Vancouver, British Columbia, Canada

Sivori D, Cattari S, Lepidi M (2022) A methodological framework to relate the earthquake-induced frequency reduction to structural damage in masonry buildings. Bull Earthq Eng 20(9):4603–4638. https://doi.org/10.1007/s10518-022-01345-8

Sumerente G, Lovon H, Tarque N, Chácara C (2020) Assessment of combined in-plane and out-of-plane fragility functions for adobe masonry buildings in the Peruvian andes. Front Built Environ 6. https://doi.org/10.3389/fbuil.2020.00052

Tondelli M, Beyer K, DeJong M (2016) Influence of boundary conditions on the out-of-plane response of brick masonry walls in buildings with RC slabs. Earthq Eng Struct Dyn 45(8):1337–1356. https://doi.org/10.1002/eqe.2710

Vaculik J (2012) Unreinforced masonry walls subjected to out-of-plane seismic actions. Ph.D. Dissertation

Vaculik J, Griffith MC (2018) Out-of-plane shaketable testing of unreinforced masonry walls in two-way bending. Bull Earthq Eng 16(7):2839–2876. https://doi.org/10.1007/s10518-017-0282-8

Van der Pluijm R (1999) Out-of-plane bending of masonry: behaviour and strength. Ph.D. Dissertation

Vanin F, Penna A, Beyer K (2020) A three-dimensional macroelement for modelling the in-plane and out-of-plane response of masonry walls. Earthq Eng Struct Dyn 49(14):1365–1387. https://doi.org/10.1002/eqe.3277

Vemuri J, Anwar T, Subramaniam KVL (2022) Seismic fragility assessment of load-bearing soft-brick unreinforced masonry piers. J Saf Sci Resilience 3(4):277–287. https://doi.org/10.1016/j.jnlssr.2022.05.001

Weyler R, Oliver J, Sain T, Cante JC (2012) On the contact domain method: a comparison of penalty and Lagrange multiplier implementations. Comput Methods Appl Mech Eng 205-208:68–82. https://doi.org/10.1016/j.cma.2011.01.011

Xie Z, Sousamli M, Messali F, Rots JG (2021) A sub-stepping iterative constitutive model for cyclic cracking-crushing-shearing in masonry interface elements. Comput Struct 257:106654. https://doi.org/10.1016/j.compstruc.2021.106654